Production of ϕ mesons at midrapidity in $\sqrt{s_{NN}} = 200$ GeV Au+Au collisions at relativistic energies

S. S. Adler,[5] S. Afanasiev,[17] C. Aidala,[5] N. N. Ajitanand,[43] Y. Akiba,[20,38] J. Alexander,[43] R. Amirikas,[12] L. Aphecetche,[45] S. H. Aronson,[5] R. Averbeck,[44] T. C. Awes,[35] R. Azmoun,[44] V. Babintsev,[15] A. Baldisseri,[10] K. N. Barish,[6] P. D. Barnes,[27] B. Bassalleck,[33] S. Bathe,[30] S. Batsouli,[9] V. Baublis,[37] A. Bazilevsky,[39,15] S. Belikov,[16,15] Y. Berdnikov,[40] S. Bhagavatula,[16] J. G. Boissevain,[27] H. Borel,[10] S. Borenstein,[25] M. L. Brooks,[27] D. S. Brown,[34] N. Bruner,[33] D. Bucher,[30] H. Buesching,[30] V. Bumazhnov,[15] G. Bunce,[5,39] J. M. Burward-Hoy,[26,44] S. Butsyk,[44] X. Camard,[45] J.-S. Chai,[18] P. Chand,[4] W. C. Chang,[2] S. Chernichenko,[15] C. Y. Chi,[9] J. Chiba,[20] M. Chiu,[9] I. J. Choi,[52] J. Choi,[19] R. K. Choudhury,[4] T. Chujo,[5] V. Cianciolo,[35] Y. Cobigo,[10] B. A. Cole,[9] P. Constantin,[16] D. G. d'Enterria,[45] G. David,[5] H. Delagrange,[45] A. Denisov,[15] A. Deshpande,[39] E. J. Desmond,[5] A. Devismes,[44] O. Dietzsch,[41] O. Drapier,[25] A. Drees,[44] R. du Rietz,[29] A. Durum,[15] D. Dutta,[4] Y. V. Efremenko,[35] K. El Chenawi,[49] A. Enokizono,[14] H. En'yo,[38,39] S. Esumi,[48] L. Ewell,[5] D. E. Fields,[33,39] F. Fleuret,[25] S. L. Fokin,[23] B. D. Fox,[39] Z. Fraenkel,[51] J. E. Frantz,[9] A. Franz,[5] A. D. Frawley,[12] S.-Y. Fung,[6] S. Garpman,[29,*] T. K. Ghosh,[49] A. Glenn,[46] G. Gogiberidze,[46] M. Gonin,[25] J. Gosset,[10] Y. Goto,[39] R. Granier de Cassagnac,[25] N. Grau,[16] S. V. Greene,[49] M. Grosse Perdekamp,[39] W. Guryn,[5] H.-Å. Gustafsson,[29] T. Hachiya,[14] J. S. Haggerty,[5] H. Hamagaki,[8] A. G. Hansen,[27] E. P. Hartouni,[26] M. Harvey,[5] R. Hayano,[8] N. Hayashi,[38] X. He,[13] M. Heffner,[26] T. K. Hemmick,[44] J. M. Heuser,[44] M. Hibino,[50] J. C. Hill,[16] W. Holzmann,[43] K. Homma,[14] B. Hong,[22] A. Hoover,[34] T. Ichihara,[38,39] V. V. Ikonnikov,[23] K. Imai,[24,38] D. Isenhower,[1] M. Ishihara,[38] M. Issah,[43] A. Isupov,[17] B. V. Jacak,[44] W. Y. Jang,[22] Y. Jeong,[19] J. Jia,[44] O. Jinnouchi,[38] B. M. Johnson,[5] S. C. Johnson,[26] K. S. Joo,[31] D. Jouan,[36] S. Kametani,[8,50] N. Kamihara,[47,38] J. H. Kang,[52] S. S. Kapoor,[4] K. Katou,[50] S. Kelly,[9] B. Khachaturov,[51] A. Khanzadeev,[37] J. Kikuchi,[50] D. H. Kim,[31] D. J. Kim,[52] D. W. Kim,[19] E. Kim,[42] G.-B. Kim,[25] H. J. Kim,[52] E. Kistenev,[5] A. Kiyomichi,[48] K. Kiyoyama,[32] C. Klein-Boesing,[30] H. Kobayashi,[38,39] L. Kochenda,[37] V. Kochetkov,[15] D. Koehler,[33] T. Kohama,[14] M. Kopytine,[44] D. Kotchetkov,[6] A. Kozlov,[51] P. J. Kroon,[5] C. H. Kuberg,[1,27] K. Kurita,[39] Y. Kuroki,[48] M. J. Kweon,[22] Y. Kwon,[52] G. S. Kyle,[34] R. Lacey,[43] V. Ladygin,[17] J. G. Lajoie,[16] A. Lebedev,[16,23] S. Leckey,[44] D. M. Lee,[27] S. Lee,[19] M. J. Leitch,[27] X. H. Li,[6] H. Lim,[42] A. Litvinenko,[17] M. X. Liu,[27] Y. Liu,[36] C. F. Maguire,[49] Y. I. Makdisi,[5] A. Malakhov,[17] V. I. Manko,[23] Y. Mao,[7,38] G. Martinez,[45] M. D. Marx,[44] H. Masui,[48] F. Matathias,[44] T. Matsumoto,[8,50] P. L. McGaughey,[27] E. Melnikov,[15] F. Messer,[44] Y. Miake,[48] J. Milan,[43] T. E. Miller,[49] A. Milov,[44,51] S. Mioduszewski,[5] R. E. Mischke,[27] G. C. Mishra,[13] J. T. Mitchell,[5] A. K. Mohanty,[4] D. P. Morrison,[5] J. M. Moss,[27] F. Mühlbacher,[44] D. Mukhopadhyay,[51] M. Muniruzzaman,[6] J. Murata,[38,39] S. Nagamiya,[20] J. L. Nagle,[9] T. Nakamura,[14] B. K. Nandi,[6] M. Nara,[48] J. Newby,[46] P. Nilsson,[29] A. S. Nyanin,[23] J. Nystrand,[29] E. O'Brien,[5] C. A. Ogilvie,[16] H. Ohnishi,[5,38] I. D. Ojha,[49,3] K. Okada,[38] M. Ono,[48] V. Onuchin,[15] A. Oskarsson,[29] I. Otterlund,[29] K. Oyama,[8] K. Ozawa,[8] D. Pal,[51] A. P. T. Palounek,[27] V. S. Pantuev,[44] V. Papavassiliou,[34] J. Park,[42] A. Parmar,[33] S. F. Pate,[34] T. Peitzmann,[30] J.-C. Peng,[27] V. Peresedov,[17] C. Pinkenburg,[5] R. P. Pisani,[5] F. Plasil,[35] M. L. Purschke,[5] A. K. Purwar,[44] J. Rak,[16] I. Ravinovich,[51] K. F. Read,[35,46] M. Reuter,[44] K. Reygers,[30] V. Riabov,[37,40] Y. Riabov,[37] G. Roche,[28] A. Romana,[25] M. Rosati,[16] P. Rosnet,[28] S. S. Ryu,[52] M. E. Sadler,[1] N. Saito,[38,39] T. Sakaguchi,[8,50] M. Sakai,[32] S. Sakai,[48] V. Samsonov,[37] L. Sanfratello,[33] R. Santo,[30] H. D. Sato,[24,38] S. Sato,[5,48] S. Sawada,[20] Y. Schutz,[45] V. Semenov,[15] R. Seto,[6] M. R. Shaw,[1,27] T. K. Shea,[5] T.-A. Shibata,[47,38] K. Shigaki,[14,20] T. Shiina,[27] C. L. Silva,[41] D. Silvermyr,[27,29] K. S. Sim,[22] C. P. Singh,[3] V. Singh,[3] M. Sivertz,[5] A. Soldatov,[15] R. A. Soltz,[26] W. E. Sondheim,[27] S. P. Sorensen,[46] I. V. Sourikova,[5] F. Staley,[10] P. W. Stankus,[35] E. Stenlund,[29] M. Stepanov,[34] A. Ster,[21] S. P. Stoll,[5] T. Sugitate,[14] J. P. Sullivan,[27] E. M. Takagui,[41] A. Taketani,[38,39] M. Tamai,[50] K. H. Tanaka,[20] Y. Tanaka,[32] K. Tanida,[38] M. J. Tannenbaum,[5] P. Tarján,[11] J. D. Tepe,[1,27] T. L. Thomas,[33] J. Tojo,[24,38] H. Torii,[24,38] R. S. Towell,[1] I. Tserruya,[51] H. Tsuruoka,[48] S. K. Tuli,[3] H. Tydesjö,[29] N. Tyurin,[15] H. W. van Hecke,[27] J. Velkovska,[5,44] M. Velkovsky,[44] V. Veszprémi,[11] L. Villatte,[46] A. A. Vinogradov,[23] M. A. Volkov,[23] E. Vznuzdaev,[37] X. R. Wang,[13] Y. Watanabe,[38,39] S. N. White,[5] F. K. Wohn,[16] C. L. Woody,[5] W. Xie,[6] Y. Yang,[7] A. Yanovich,[15] S. Yokkaichi,[38,39] G. R. Young,[35] I. E. Yushmanov,[23] W. A. Zajc,[9,†] C. Zhang,[9] S. Zhou,[7] S. J. Zhou,[51] and L. Zolin[17]

(PHENIX Collaboration)

[1]*Abilene Christian University, Abilene, Texas 79699, USA*

[2]*Institute of Physics, Academia Sinica, Taipei 11529, Taiwan*

[3]*Department of Physics, Banaras Hindu University, Varanasi 221005, India*

[4]*Bhabha Atomic Research Centre, Bombay 400 085, India*

[5]*Brookhaven National Laboratory, Upton, New York 11973-5000, USA*

[6]*University of California, Riverside, California 92521, USA*

[7]*China Institute of Atomic Energy (CIAE), Beijing, People's Republic of China*

[8]*Center for Nuclear Study, Graduate School of Science, University of Tokyo, 7-3-1 Hongo, Bunkyo, Tokyo 113-0033, Japan*

[9]*Columbia University, New York, New York 10027 and Nevis Laboratories, Irvington, New York 10533, USA*

*Deceased.

†PHENIX Spokesperson: zajc@nevis.columbia.edu

[10]*Dapnia, CEA Saclay, F-91191 Gif-sur-Yvette, France*
[11]*Debrecen University, Egyetem tér 1, H-4010 Debrecen, Hungary*
[12]*Florida State University, Tallahassee, Florida 32306, USA*
[13]*Georgia State University, Atlanta, Georgia 30303, USA*
[14]*Hiroshima University, Kagamiyama, Higashi-Hiroshima 739-8526, Japan*
[15]*Institute for High Energy Physics (IHEP), Protvino, Russia*
[16]*Iowa State University, Ames, Iowa 50011, USA*
[17]*Joint Institute for Nuclear Research, 141980 Dubna, Moscow Region, Russia*
[18]*KAERI, Cyclotron Application Laboratory, Seoul, South Korea*
[19]*Kangnung National University, Kangnung 210-702, South Korea*
[20]*KEK, High Energy Accelerator Research Organization, Tsukuba-shi, Ibaraki-ken 305-0801, Japan*
[21]*KFKI Research Institute for Particle and Nuclear Physics (RMKI), Post Office Box 49, H-1525 Budapest 114, Hungary*
[22]*Korea University, Seoul, 136-701, Korea*
[23]*Russian Research Center "Kurchatov Institute," Moscow, Russia*
[24]*Kyoto University, Kyoto 606-8502, Japan*
[25]*Laboratoire Leprince-Ringuet, Ecole Polytechnique, CNRS-IN2P3, Route de Saclay, F-91128 Palaiseau, France*
[26]*Lawrence Livermore National Laboratory, Livermore, California 94550, USA*
[27]*Los Alamos National Laboratory, Los Alamos, New Mexico 87545, USA*
[28]*LPC, Université Blaise Pascal, CNRS-IN2P3, Clermont-Fd, F-63177 Aubiere Cedex, France*
[29]*Department of Physics, Lund University, Box 118, SE-221 00 Lund, Sweden*
[30]*Institut für Kernphysik, University of Muenster, D-48149 Muenster, Germany*
[31]*Myongji University, Yongin, Kyonggido 449-728, Korea*
[32]*Nagasaki Institute of Applied Science, Nagasaki-shi, Nagasaki 851-0193, Japan*
[33]*University of New Mexico, Albuquerque, New Mexico 87131, USA*
[34]*New Mexico State University, Las Cruces, New Mexico 88003, USA*
[35]*Oak Ridge National Laboratory, Oak Ridge, Tennessee 37831, USA*
[36]*IPN-Orsay, Universite Paris Sud, CNRS-IN2P3, BP1, F-91406 Orsay, France*
[37]*PNPI, Petersburg Nuclear Physics Institute, Gatchina, Russia*
[38]*RIKEN (The Institute of Physical and Chemical Research), Wako, Saitama 351-0198, Japan*
[39]*RIKEN BNL Research Center, Brookhaven National Laboratory, Upton, New York 11973-5000, USA*
[40]*St. Petersburg State Technical University, St. Petersburg, Russia*
[41]*Universidade de São Paulo, Instituto de Física, Caixa Postal 66318, São Paulo CEP05315-970, Brazil*
[42]*System Electronics Laboratory, Seoul National University, Seoul, South Korea*
[43]*Chemistry Department, Stony Brook University, SUNY, Stony Brook, New York 11794-3400, USA*
[44]*Department of Physics and Astronomy, Stony Brook University, SUNY, Stony Brook, New York 11794, USA*
[45]*SUBATECH (Ecole des Mines de Nantes, CNRS-IN2P3, Université de Nantes) Bôite Postale 20722, F-44307 Nantes, France*
[46]*University of Tennessee, Knoxville, Tennessee 37996, USA*
[47]*Department of Physics, Tokyo Institute of Technology, Tokyo 152-8551, Japan*
[48]*Institute of Physics, University of Tsukuba, Tsukuba, Ibaraki 305, Japan*
[49]*Vanderbilt University, Nashville, Tennessee 37235, USA*
[50]*Waseda University, Advanced Research Institute for Science and Engineering, 17 Kikui-cho, Shinjuku-ku, Tokyo 162-0044, Japan*
[51]*Weizmann Institute, Rehovot 76100, Israel*
[52]*Yonsei University, IPAP, Seoul 120-749, Korea*
(Received 8 October 2004; published 14 July 2005)

We present the results of ϕ meson production in the K^+K^- decay channel from Au+Au collisions at $\sqrt{s_{NN}} = 200$ GeV as measured at midrapidity by the PHENIX detector at Brookhaven National Laboratory's Relativistic Heavy Ion Collider. Precision resonance centroid and width values are extracted as a function of collision centrality. No significant variation from the Particle Data Group accepted values is observed, contrary to some model predictions. The ϕ transverse mass spectra are fitted with a linear exponential function for which the derived inverse slope parameter is seen to be constant as a function of centrality. However, when these data are fitted by a hydrodynamic model the result is that the centrality-dependent freeze-out temperature and the expansion velocity values are consistent with the values previously derived from fitting identified charged hadron data. As a function of transverse momentum the collisions scaled peripheral-to-central yield ratio R_{CP} for the ϕ is comparable to that of pions rather than that of protons. This result lends support to theoretical models that distinguish between baryons and mesons instead of particle mass for explaining the anomalous (anti) proton yield.

DOI: 10.1103/PhysRevC.72.014903 PACS number(s): 25.75.Dw

I. INTRODUCTION

Relativistic heavy-ion experiments have a goal of producing matter at extreme temperatures and energy densities such that conditions are favorable for the transition to a deconfined state of quarks and gluons, the quark gluon plasma (QGP). Theoretical calculations predict that the temperatures and energy densities that can be reached at the Brookhaven National Laboratory's Relativistic Heavy Ion Collider (RHIC) will exceed those needed for the formation of the QGP [1–3].

The production and decay of the ϕ meson have long been recognized as an important probe for the state of matter produced in relativistic heavy-ion (RHI) collisions [4–21]. In pp collisions the creation of the ϕ is suppressed according to the Okubo-Zweig-Iizuka rule [22]. Hence, if there is an enhancement of the ϕ yield in RHI collisions relative to pp collisions, this could be evidence of nonconventional production mechanisms such as strange quark coalescence via the formation and subsequent hadronization of the QGP. The fact that the ϕ yield is undistorted by feed-down from higher mass resonances makes it an attractive probe in this respect.

The decay modes of the ϕ, specifically the dilepton channels (e^+e^- or $\mu^+\mu^-$) and the K^+K^- channel, will probe the final state differently should the decay take place in the presence of the QGP-mixed or the completely hadronized phase. The dileptons will have insignificant interactions with the medium, whereas the kaons can scatter until freeze-out. The lifetime of the ϕ in vacuum is large ($\approx$45 fm/c) compared to say a 10-fm-sized interaction region. However, several theoretical calculations [13,21,23] predict that the ϕ mass and width could be significantly modified in either the hot or the cold nuclear medium. These medium-induced effects could be manifested through measured shifts in the mass centroid of the resonance or changes in the resonance width. Also predicted are changes in the relative branching ratio between kaon and lepton pairs, with respect to the Particle Data Group (PDG) [24].

The production mechanism of strangeness in heavy-ion collisions can be investigated through the measurement of the particle yields. In this paper, we study system size dependence by analyzing centrality-selected data. A comparison between different systems can be made by normalizing to the number of participant pairs. The expectation is that for production dominated by soft processes, the yields scale as the number of participants. We compare the centrality dependence of strange and nonstrange particle yields to reveal a possible flavor dependence.

An additional important question is whether the ϕ mesons participate in radial flow together with the other hadrons, or if they freeze-out earlier, as might be true if the small vacuum cross sections of the ϕ with hadrons persist in the fireball. Previous measurements have yielded contradictory results [25, 26]. One of the important advantages of RHIC experiments is the capability to examine the momentum spectrum as a function of centrality for a variety of hadrons, which should yield important additional information on the radial flow issue. A spectral shape analysis including a simultaneous treatment of the ϕ and the more abundant hadrons (π, K, p) will be presented here.

At high p_T, hadrons are primarily produced from the fragmentation of hard-scattered partons. One of the most exciting results from RHIC was the discovery of hadron suppression in central Au+Au collisions [27,28]; this suppression is absent in d + Au collisions [29]. Surprisingly, it was also discovered that proton and antiproton production at intermediate p_T (1.5–4.5 GeV/c) scales with the number of binary nucleon-nucleon collisions ($N_{\rm coll}$) as would be expected for hard scattering in the absence of any nuclear modification [30]. In fact, the intermediate p_T antiproton to pion ratios were found to exceed by a factor of 3 the values expected from parton fragmentation [30,31]. These experimental results lead to the conclusion that protons and pions have different production mechanisms at intermediate p_T [30]. One possible explanation invokes parton recombination from the QGP [32–35]. A measurement of the nuclear modification factor for the ϕ meson, which has a mass comparable to the proton but carries only two quarks, is crucial for understanding the hadron production at intermediate p_T. In this work we have measured the nuclear modification factor through the ratio $R_{\rm CP}$ of central to peripheral yields scaled by their respective $N_{\rm coll}$ value.

To put our results into perspective, we begin by describing the currently available ϕ data obtained in RHI collisions. The production of ϕ mesons has been studied systematically at ever increasing $\sqrt{s}$ from the AGS to RHIC. The E802 collaboration made the first observation of the ϕ in fixed-target central collisions of 14.6A GeV Si+Au ($\sqrt{s_{NN}} = 5.39$ GeV) via the K^+K^- channel [36]. They obtained a ratio $N_\phi/N_{K^-} = 11.6\%$, roughly consistent with the ratio obtained in pp data over a wide range of $\sqrt{s}$ [37]. The analysis of the E802 rapidity distributions indicated that the ϕ production scaled with the product of the K^+ and K^- separate yields and that either there was significant rescattering of the ϕ after production or the production itself came after rescattering of the colliding participants.

Also at the AGS the E917 experiment has reported another ϕ measurement with 11.7A GeV Au+Au ($\sqrt{s_{NN}} = 4.87$ GeV) in the rapidity range $1.2 < y < 1.6$ in five centrality bins [38]. The observed yield of the ϕ increased toward more central collisions with a distinctly greater than linear dependence on the number of participants. The yield increase of the ϕ in central collisions was stronger than that of the π since the N_ϕ/N_π ratio increased in central collisions. However, the N_ϕ/N_{K^+} and N_ϕ/N_{K^-} ratios were constant as a function of centrality.

At the SPS the NA49 experiment has measured ϕ production in pp, p+Pb, and Pb+Pb collisions with $E_{\rm beam} =$ 158A GeV ($\sqrt{s_{NN}} = 17.5$ GeV) in the rapidity range $3.0 < y < 3.8$ [39]. Relative to the pp yields, these data showed that the ratio of the ϕ yield to the π yield in central Pb+Pb collisions was enhanced by a factor of 3.0 ± 0.7. Another SPS collaboration, NA38/NA50, has measured the ϕ in the $\mu^+\mu^-$ channel [40,41], for which the extracted effective temperature and dN/dy differ from those obtained in the K^+K^- channel in the same systems. The yield difference between the two SPS experiments has been calculated to be factors of 2–4 [42], with the NA38/NA50 result being higher.

The first measurement of the ϕ meson at RHIC was reported by the STAR Collaboration [43], in the collisions of Au+Au

at $\sqrt{s_{NN}} = 130$ GeV at three centralities, 0–11%, 11–26%, and 26–85%, in the rapidity range $-0.5 < y < +0.5$. The extracted temperature T and the ratio $N_\phi/N_{\text{hadrons}}$ did not vary with centrality.

One may summarize the current state of knowledge on ϕ production in heavy-ion collisions by stating that the topic remains highly unexplored territory. The heavy-ion measurements do indicate that the observed ϕ yield is not a simple linear superposition of nucleon-nucleon collisions. Rather, the data imply the influence of some collective effects. Whether those effects are induced by cold and/or hot nuclear matter is not known since there does not yet exist definitive evidence. Moreover, thus far there has not been precise enough heavy-ion data that can address the question of the change in the ϕ mass or its width in the cold nuclear or the hot QGP medium. And except for one experiment measuring the dimuon channel, there is a scarcity of useful quantitative information in heavy-ion collisions concerning the ϕ decay into dileptons.

In this paper we report on a measurement of the ϕ yield at midrapidity in collisions of Au+Au beams from RHIC at $\sqrt{s_{NN}} = 200$ GeV as measured in the K^+K^- channel by the PHENIX detector. The paper is organized as follows. In Sec. II we give a short review of the PHENIX detector configuration. In Sec. III we describe the data analysis procedure. Section IV presents and discusses the results. The first precision measurements of ϕ mass and width values obtained in RHI collisions as a function of centrality are given in Sec. IV A. Absolute yields as a function of p_T for three centrality bins are shown in Sec. IV B. The centrality dependence of yields and ratios are studied in Sec. IV D. In Sec. IV D the spectra shapes are interpreted in the framework of a hydrodynamical model and the freeze-out conditions are extracted. Finally, the nuclear modification factor R_{CP} for the ϕ is obtained and compared to those of pions and protons in Sec. IV E.

II. PHENIX DETECTOR

The PHENIX detector consists of two spectrometer arms at near zero rapidity, two forward rapidity muon spectrometers, and three global event characterization detectors. The central arm spectrometers, shown schematically in Fig. 1, are located east and west of the beam line with $\pi/2$ radian azimuthal coverage each. These spectrometers are designed to detect photons, electrons, and charged hadrons. The ϕ data for this paper were obtained with the central arm detector subsystems, which provide high-resolution particle identification and momentum reconstruction. A complete description of the PHENIX apparatus has been published elsewhere [44–49]. We present a brief review of the relevant detector subsystems in the following sections.

A. Global detectors

The global detectors furnish the start time signals, collision vertex measurements, and interaction centrality. The centrality for events in the Au+Au collisions is determined [50] by combining the data from two subsystems: the zero degree calorimeters (ZDC) [48] and the beam-beam counters (BBC)

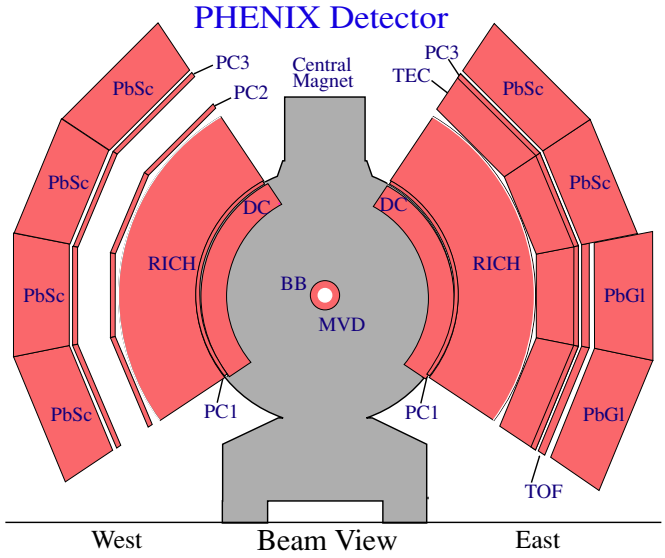

FIG. 1. (Color online) Beam's-eye view of the PHENIX central arm detector subsystems.

[47]. The ZDC are hadronic calorimeters located 18 m downstream and upstream of the interaction point along the beam line. These calorimeters detect the energy carried by spectator neutrons. The BBC are Čerenkov telescopes placed ± 1.44 m from the center of the beam collision region in the pseudorapidity region $3.0 < |\eta| < 3.9$. The correlation between the ZDC energy sum and the charge sum recorded in the BBC determines the centrality of the collision event. The BBC data also determine the longitudinal collision coordinate (z_{vertex}) and the start time for the time-of-flight measurements.

B. Central arm detectors

The central arm spectrometers [49] in PHENIX provide charged particle tracking and particle identification. This analysis was done with the east arm spectrometer. The $\phi \to K^+K^-$ decay kinematics are such that that the PHENIX detector has negligible acceptance for the very low p_T ϕ particles, which would decay into east-west kaon pairs. The data included information from the drift chamber (DC), the pad chambers (PC1 and PC3), the high-resolution time-of-flight (TOF) wall, and the electromagnetic calorimeter (EMCal) lead-scintillator detectors (PbSc), as depicted in Fig. 1.

Pattern recognition and tracking of the charged particles are accomplished using the DC information by a combinatorial Hough transform method [51]. The DC subsystem is located at an average radial distance of 2.2 m from the beam line. It is a projective tracking detector providing high-precision measurements in the azimuthal XY plane, which are combined with the XYZ single spatial point measurement from the PC1 located at 2.45 m. These data, together with the BBC z_{vertex} information, are sufficient to determine the track's initial momentum vector, whose magnitude is obtained with a resolution $\delta p/p \simeq 0.7\% \oplus 1.0\% \times p$ (GeV/c). The first term in this expression is due to the multiple scattering before the DC and the second term is the angular resolution of the DC.

Based on identified mass measurements obtained with the TOF subsystem, the absolute momentum scale is known to $\pm 0.7\%$.

Tracks obtained from the DC/PC1 detectors are projected to the PC3, TOF, and PbSc detectors where associations can be made. The high-resolution TOF subsystem provides one set of mass measurements while the PbSc detectors provide a geometrically independent set of mass measurements. The TOF wall is positioned 5.06 m from the beam line and consists of 960 scintillator slats oriented along the azimuthal direction. It is designed to cover $|\eta| < 0.35$ and $\Delta\phi = \pi/4$ in azimuthal angle.

The PbSc detector, covering half of the east arm and entire west arm, can also be used for hadron timing measurements. The present analysis uses the PbSc modules in the east arm, which are located at 5.1 m in radial distance from the beam line and cover a $\Delta\phi = \pi/4$ azimuthal range. This detector is constructed as separate towers of dimension $5.25 \times 5.25 \times 37\ \mathrm{cm}^3$, in an alternating lead-scintillator sandwich-type structure ("shish-kebob"), approximately 18 radiation lengths in depth. As illustrated in Fig. 1 the TOF and the PbSc sectors are completely nonoverlapping.

III. DATA ANALYSIS

In this section, we describe the event and track selection, particle identification, the details of K^+K^- pair reconstruction, and the corrections for geometrical acceptance, particle decay in flight, multiple scattering, and detector occupancy factors, all of which couple into deriving the ϕ meson spectra.

A. Event selection

The events selected for this analysis were based on the PHENIX minimum-bias trigger provided by the BBC and ZDC. As noted previously, the centrality of each Au+Au collision event was determined by correlating the BBC charge sum and the ZDC total energy [50]. The PHENIX minimum-bias data sample included $92.2^{+2.5}_{-3.0}\%$ of the 6.9-b Au+Au total inelastic cross section [29]. This analysis used 20 million minimum-bias events with a vertex position within $|z_{\mathrm{vertex}}| < 30$ cm.

To study the centrality-dependent physics, we divided these events into different centrality bins. For the ϕ meson lineshape analysis, we used five centrality bins: 0–10%, 10–20%, 20–40%, 40–60%, and 60–92%. The transverse mass (m_T) spectra were reconstructed for three centrality bins: 0–10%, 10–40%, and 40–92%. These bin divisions were chosen to have approximately equal statistical significance for their respective data points. The centrality of collisions is additionally characterized by the average number of participants ($\langle N_{\mathrm{part}} \rangle$) and the average number of binary nucleon–nucleon collisions ($\langle N_{\mathrm{coll}} \rangle$). These two global quantities, shown in Table I as a function of centrality, are derived from a Glauber model calculation [29].

B. Track selection

Only tracks with valid information from the DC and the PC1 were used for the analysis. These tracks were then confirmed by matching the projected and associated hit information at the TOF wall for the TOF analysis, or at the PC3 and the EMCal for the PbSc analysis. The differences between the actual azimuthal and longitudinal hit coordinates compared to the projected hit coordinates were determined. These tracking coordinate residuals were converted to standard deviation residuals by a momentum-dependent function that computed the expected residual coordinate value. On this basis, a 3σ track-matching cut was used to accept track associations. Lastly, for the TOF wall, an energy-loss cut is applied on the analog signal height from the scintillator slat. This cut has been described in a previous publication [50].

TABLE I. Average number of participants and collisions in Au+Au reaction at RHIC for different centralities determined from a Glauber model [29]. The error associated with each number is the systematic error.

Centrality (%)	$\langle N_{\mathrm{part}} \rangle$	$\langle N_{\mathrm{coll}} \rangle$
0–10	325.2 ± 3.3	955.4 ± 93.6
10–20	234.6 ± 4.7	602.6 ± 59.3
20–40	140.4 ± 4.9	296.8 ± 31.1
10–40	171.8 ± 4.8	398.7 ± 40.5
40–60	59.9 ± 3.5	90.6 ± 11.8
60–92	14.5 ± 2.5	14.5 ± 4.0
40–92	32.0 ± 2.9	45.2 ± 7.3
Minimum Bias	109.1 ± 4.1	257.8 ± 25.4

C. Particle identification

As mentioned earlier, the PHENIX central arm spectrometer utilizes the high-resolution TOF wall and PbSc modules for hadron mass identification. The kaons in the TOF wall were identified via reconstructed momentum combined with a TOF measurement. The timing resolution of this subsystem is $\sigma \simeq 115$ ps. A momentum range of 0.3–2.0 GeV/c was selected to compute the mass distributions [52]. Figure 2 shows the mass-squared distribution of all tracks passing through the TOF module for six different momentum bins. The kaons were identified by applying a 2σ mass-squared cut, which is shown by the shaded region in each plot.

The particle identification with the electromagnetic calorimeter modules is sensitive to the fact that the electromagnetic and hadronic interactions produce quite different patterns of energy sharing between calorimeter towers [53]. As a consequence, the hadron timing properties of the PbSc depend on the energy deposited on the central tower of the cluster, particle momentum, particle type, charge, angle of incidence of the track, etc. The PbSc hadronic timing response was corrected for these effects and we obtained an overall timing resolution of $\sigma \simeq 450$ ps, which is sufficient to enable a clear π/K separation within $0.3 < p(\mathrm{GeV/c}) < 1.0$ using a 2σ mass-squared selection criterion. In Fig. 3 the mass-squared distributions are plotted for four different momentum slices for all tracks passing through PC3 and PbSc. The identified kaons are also shown in the figure by the 2σ width shaded histograms superimposed on the M^2 distributions for all tracks in different momentum bins.

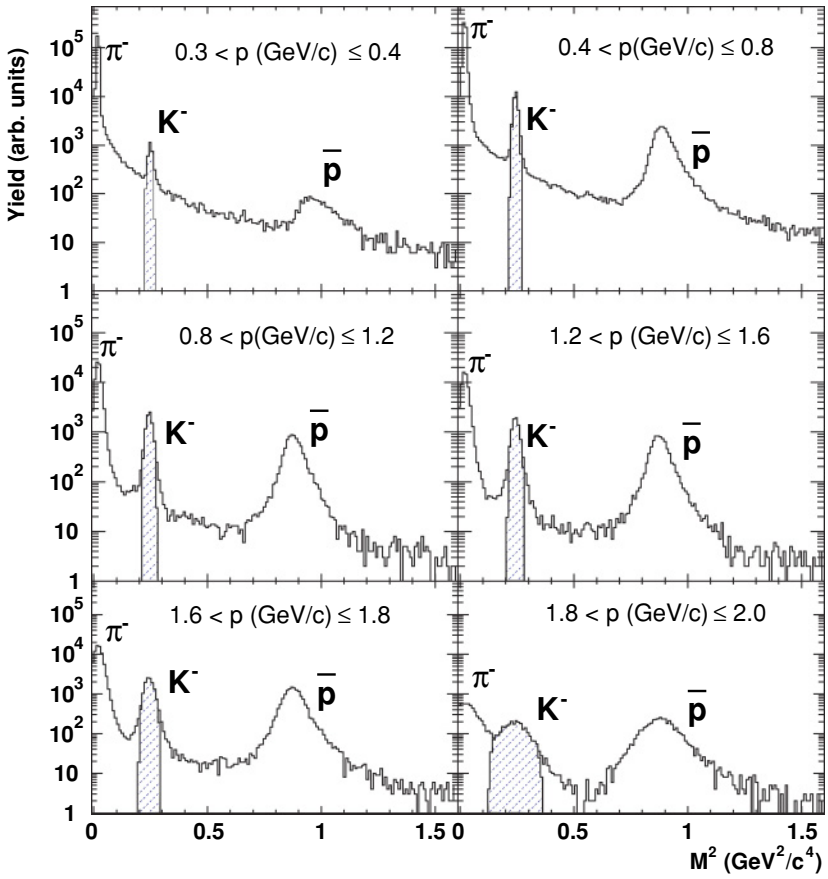

FIG. 2. (Color online) Mass-squared distribution of all accepted tracks passing through the TOF for six selected momentum bins. The identified kaons within 2σ mass-squared boundaries at the different momentum bins are shown by the shaded region on each plot.

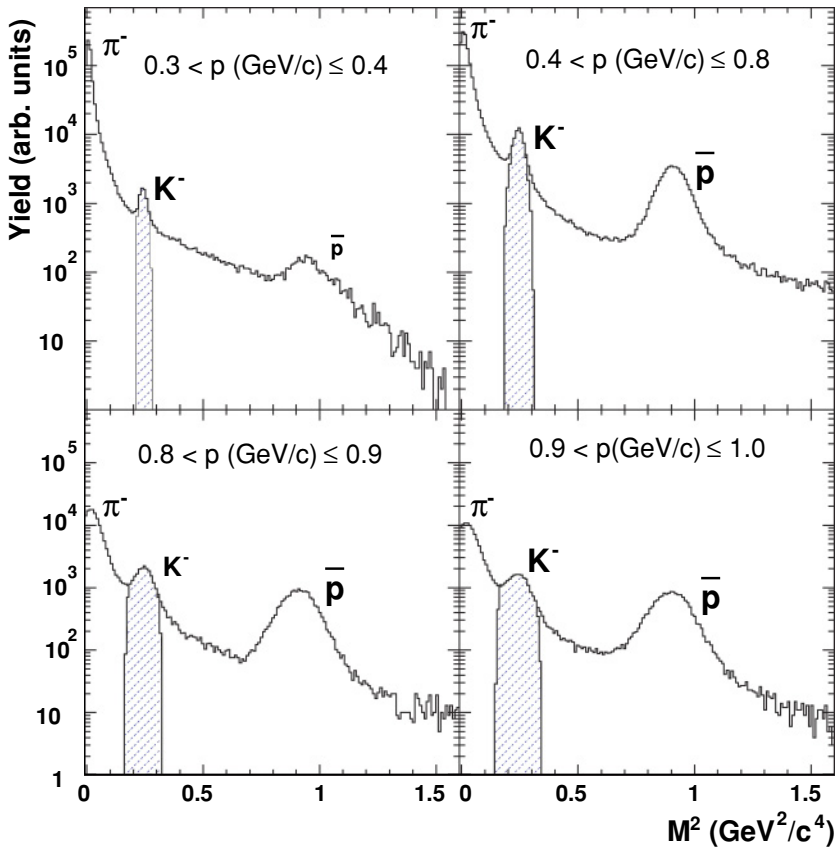

FIG. 3. (Color online) Mass-squared distribution of all selected tracks passing through the PbSc for four momentum bins. The identified kaons within 2σ mass-squared boundaries at the different momentum bins are shown by the shaded region on each plot.

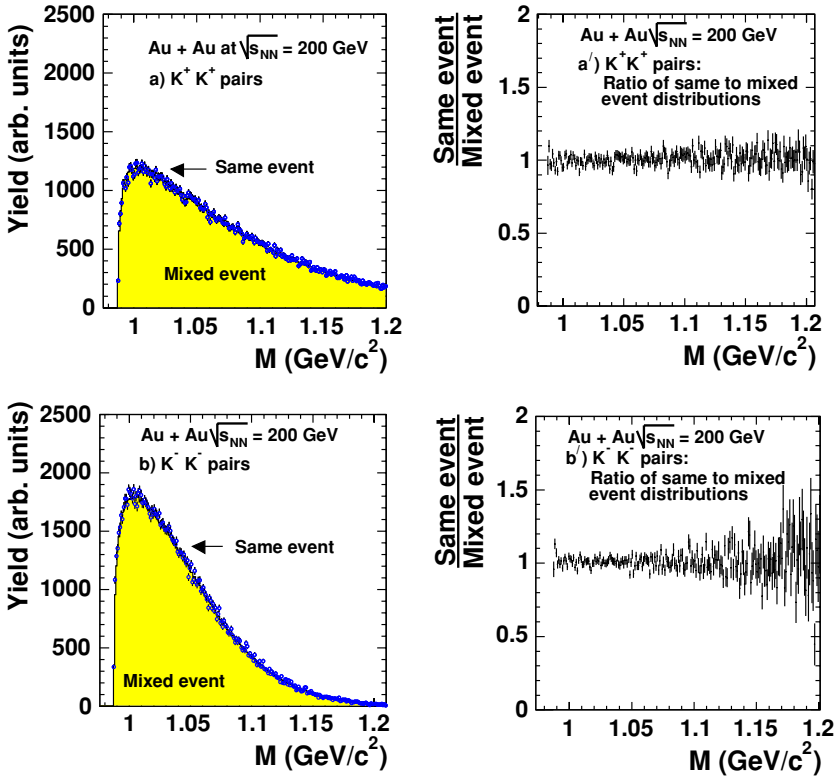

FIG. 4. (Color online) K^+K^+ [(a) and (a′)] and K^-K^- [(b) and (b′)] invariant mass spectra and ratio of real to mixed event spectra, respectively, for the TOF-PbSc combination.

D. K^+K^- invariant mass spectra and ϕ signal extraction

All identified K^+ and K^- tracks in a given event were combined to form the invariant pair mass distributions. Three different pair combinations were used:

(a) both K^+ and K^- identified by the TOF detector (TOF-TOF combination),
(b) K^+ identified with TOF and K^- identified with the PbSc detector (TOF-PbSc combination), and
(c) both K^+ and K^- identified with the PbSc detector (PbSc-PbSc combination).

We did not use the K^+ from PbSc and K^- from TOF in the (b) combination. This is because the PHENIX central arm geometry, in the presence of a 0.8 T m magnetic field, does not have any acceptance for such pairs below an invariant mass of 1.06 GeV/c^2 in the TOF-PbSc combination.

A large combinatorial background is inherent to the K^+K^- pair invariant mass distribution. The combinatorial background was estimated by an event-mixing method in which all K^+ tracks from one event were combined with K^- tracks of ten other events within the same centrality and vertex class. The mixed-event technique reproduces the shape of the unlike-sign combinatorial background. Finally, the size of the combinatorial background is obtained by normalizing the mixed-event invariant mass spectra to $2\sqrt{N_{++}N_{--}}$, where N_{++} and N_{--} represent the measured yields in K^+K^+ and K^-K^- mass distributions, respectively. This normalization is derived analytically starting from the assumption that the number of $K^\pm$ tracks per event-follows a Poisson distribution. A complete derivation of this is given in Appendix A.

The ability of this event-mixing method to reproduce correctly the shape of the combinatorial background distribution was confirmed by constructing, in a similar way, the mixed-event like-sign spectrum and comparing it to the same-event like-sign pair distribution. The assumption is that the like-sign pair distributions are purely combinatoric. For the three detector combinations, TOF-TOF, TOF-PbSc, and PbSc-PbSc, the ratio of the measured and combinatorial like-sign invariant mass distributions were found to be consistent with 1.0 as a function of the pair mass within statistical errors for all centrality bins. As an example, in Fig. 4 we plot the measured and combinatorial "$+\,+$" and "$-\,-$" invariant mass distributions and their ratios for the TOF-PbSc combination as a function of the invariant mass of K^+K^+ and K^-K^- pairs for minimum-bias events. As can be seen from the figures, these ratios are equal to the expected value of 1.0 within the statistical fluctuations.

The systematic uncertainty associated with this normalization procedure was estimated to vary between 0.5% and 2% for the different centralities in the different detector combinations. When we added all data together to derive the ϕ spectrum, the range of the systematic uncertainty is reduced to 0.7–1.0%.

Finally, the ϕ meson signal was obtained by subtracting the combinatorial background from the measured unlike-sign invariant mass spectrum. An example of the K^+K^- invariant mass spectrum for the TOF-PbSc combination is shown in Fig. 5, where we plotted the measured and scaled mixed-event invariant mass distributions for minimum-bias events. The lower panel of the figure shows the subtracted mass spectrum. The corrected yield of the ϕ mesons from the experimental data is then determined by integrating the subtracted invariant

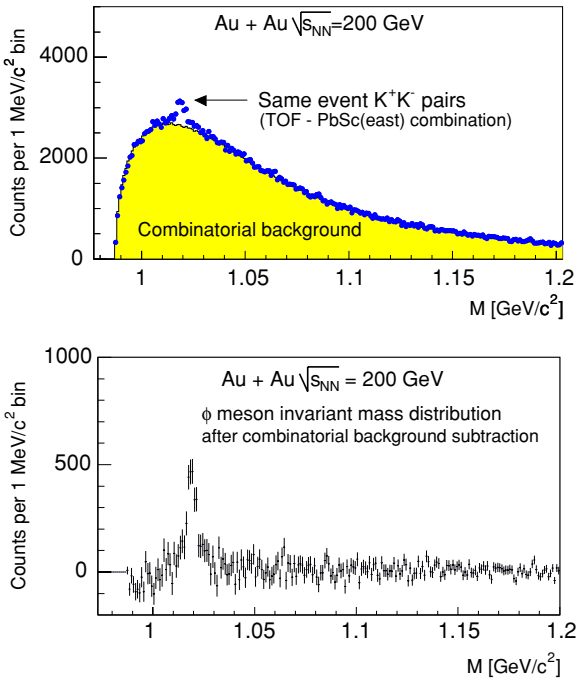

FIG. 5. (Color online) K^+K^- invariant mass spectra for the measured and mixed events (top) in the TOF-PbSc combination, and the subtracted mass spectrum showing the ϕ meson peak clearly above the background (bottom).

mass spectrum within a mass window of $\pm 5\,\mathrm{MeV}/c^2$ about the measured ϕ mass centroid. This narrow mass window was used as it provided a better signal-to-background ratio compared with a wider window. Since we will show that there is no significant centrality dependence of the intrinsic width, then the extracted yields as a function of centrality are not being biased by the use of a constant integration window. The systematic effect of the mass integration window itself on the corrected yield was studied by varying the stated integration limit and was found to contribute 2.6–3.2%, depending on centrality, to the total systematic uncertainty in the integrated yield.

E. Acceptance, decay, and multiple-scattering corrections

The ϕ meson yields were corrected for the geometrical acceptance of the detectors, in-flight kaon decay, multiple-scattering effects, and nuclear interactions with materials in the detector using the PISA software package, which is a GEANT-based [54] Monte Carlo detector simulation of the PHENIX detector. The simulation was carried out by generating 34 million single ϕ mesons in a ± 0.6 rapidity interval with an exponential transverse momentum distribution

$$dN/dp_T = p_T \exp[-m_T/(t_{\mathrm{fo}} + \beta^2 M_\phi)] \qquad (1)$$

with $t_{\mathrm{fo}} = 157$ MeV and $\beta = 0.4$, that is, an effective slope of $T = 320$ MeV in the range $0 < p_T < 10$ GeV/c. The generated ϕ mesons were then propagated through the simulation package. In this simulation, the BBC, DC, PC, TOF, and PbSc detector responses were tuned to match the real data by including their dead areas and by matching their track

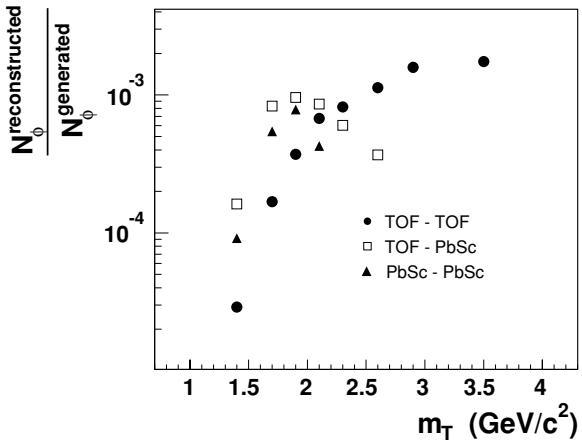

FIG. 6. Detector acceptance efficiency vs transverse mass of the simulated K^+K^- pairs for the TOF-TOF, TOF-PbSc, and PbSc-PbSc combinations. The statistical errors are smaller than the size of the data symbols.

associations and mass-squared resolutions. That is, the track association and mass-squared cut boundaries in the Monte Carlo analysis were parametrized to match the real data. The K^+K^- pair acceptance efficiency as a function of transverse mass was calculated as

$$\epsilon(m_T) = \frac{N_\phi^{\mathrm{reconstructed}}(m_T)}{N_\phi^{\mathrm{generated}}(m_T)}. \qquad (2)$$

The calculated acceptance efficiencies for the TOF-TOF, TOF-PbSc, and PbSc-PbSc combinations are shown in Fig. 6 as a function of m_T. The points in the figure are located at the center of the bins. In the actual m_T spectra, the proper bin centroids were used. The figure shows that the TOF detector (closed circles) has low acceptance for the low-momentum kaon pairs owing to their large opening angles. However, the TOF covers the largest m_T range for the ϕ particles. As a result, the TOF efficiency function increases toward higher transverse mass. In contrast, the TOF-PbSc (open squares) and PbSc-PbSc (closed triangles) combinations offer better low-pair-momentum acceptance than the TOF. However, the high-momentum kaon identification limit in the PbSc leads to the efficiency function decreasing at the highest transverse mass values.

To check the sensitivity of the acceptance correction factors to the input inverse slope of the ϕ mesons, the acceptance corrections are calculated for two input inverse slope parameters, $T = 320$ and 440 MeV. Both are found to be almost consistent within $\sim$1% uncertainty as a function of the momentum of the generated ϕ mesons. This is added as a systematic uncertainty to the acceptance correction factor.

In general, the PHENIX east arm ($|\eta| < 0.35$) particle identification detectors, in the presence of the central arm magnetic field, accepts 0.5% of the $\phi \to K^+K^-$ pairs generated within $|y| < 0.5$ and $1.2 < m_T^\phi(\mathrm{GeV}/c^2) < 4.0$. The factors that influence this geometrical acceptance are the geometry of TOF and PbSc at the PHENIX east arm, in-flight kaon decay, multiple-scattering effects, nuclear interactions of the kaons with detector materials, and the central arm magnetic

field. Out of those, about 17% of the kaon pairs are finally reconstructed after single-track reconstruction, track selection criteria, particle identification cuts, and finally the ϕ meson reconstruction within ± 5 MeV mass window with respect to its centroid.

The systematic error associated with the acceptance correction factor originates from

(i) tuning of detector alignments and mass-squared parameters in the Monte Carlo with reference to the real data ($\sim$3%),
(ii) systematics in the fiducial geometries in the data and the Monte Carlo ($\sim$12%), and
(iii) variation of the input inverse slope of the event generator ($\sim$1%).

F. Detector-occupancy correction

The high-multiplicity environment in the heavy-ion collisions produces multiple hits in a detector cell such as in the slats of the TOF or in the towers of the PbSc. These occupancy effects reduce the track reconstruction efficiency in central collisions compared to that in peripheral collisions, and these occupancy-dependent effects need to accounted for in calculating the invariant yields. The multiplicity-dependent efficiency ($\epsilon_{\text{occupancy}}$) factors were calculated by embedding simulated K^+K^- pairs into real data events. This study was done for different centrality bins from 0 to 92% in steps of 10%. We calculated the multiplicity-dependent efficiencies for TOF-TOF, TOF-PbSc, and PbSc-PbSc pairs separately. The systematic uncertainty associated with the embedding procedure was estimated for the three centrality bins used in the yield determinations, namely, 0–10%, 10–40%, and 40–92%. The systematic errors, calculated by estimating the occupancy-efficiency corrections for different track-confirming criteria, were found to vary from 7% to 10% for the three centrality bins used here, independent of the pair momenta. Figure 7 shows the $\epsilon_{\text{occupancy}}$ factors as a function of collision centrality

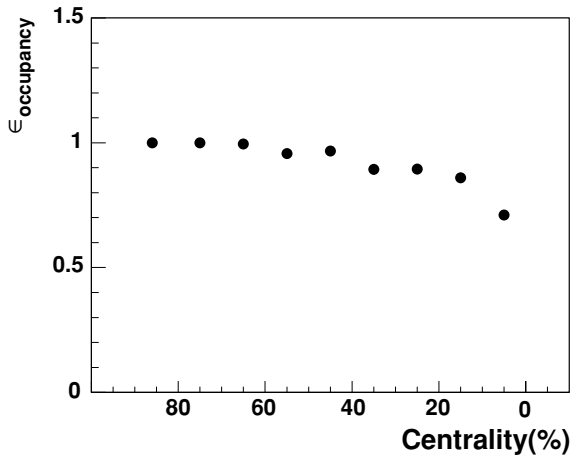

FIG. 7. Multiplicity-(occupancy-)dependent efficiency correction for detecting the ϕ meson in the PHENIX detector as a function of the collision centrality. The most central collisions are to the right; the most peripheral collisions are to the left. The statistical errors are less than the size of the data points.

for the K^+K^- pairs both identified in the TOF detector. The occupancy-dependent efficiency factors were found to be independent of the transverse momenta of the pairs.

IV. RESULTS AND DISCUSSION

In this section, we present and discuss the results of our measurements, which consist of (1) the ϕ line-shape analysis, (2) the transverse mass spectra analysis, (3) the integrated yields and ratios analysis, (4) hydrodynamical fits to $\pi^{\pm}$, $K^{\pm}$, p, $\overline{p}$, and ϕ transverse momentum spectra, and (5) the centrality dependence of the yields and nuclear modification factor R_{CP} as compared to that of pions and (anti)protons.

A. Line-shape analysis

The invariant mass spectra of the ϕ mesons are obtained by subtracting the combinatorial backgrounds from the same event K^+K^- mass spectra. The details of the combinatorial background analysis were described in Sec. III D. For the best statistical precision, we combine data from TOF and PbSc detectors to analyze the ϕ mass centroids and widths at the five different centrality bins. This is done by simply adding the measured and combinatorial invariant mass spectra from the three independent subsystem combinations mentioned in Sec. III D and then subtracting the total combinatorial background from the total measured mass spectra.

Figure 8 shows the minimum-bias $\phi \rightarrow K^+K^-$ invariant mass spectrum for the PHENIX data. The subtracted ϕ mass

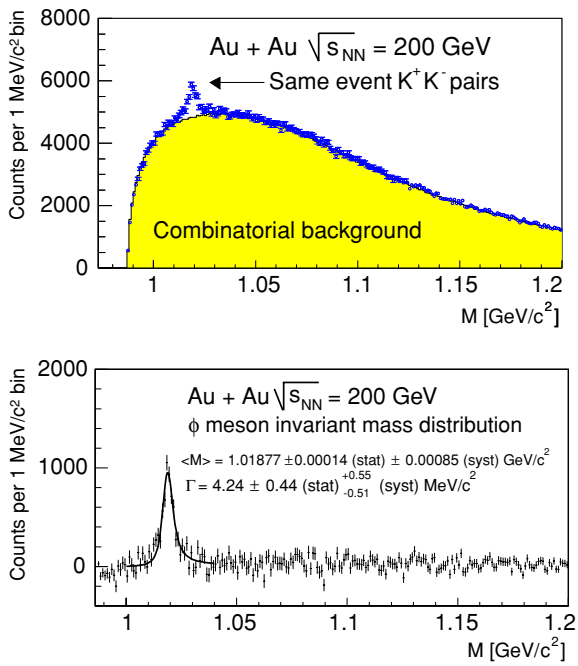

FIG. 8. (Color online) Minimum-bias $\phi \rightarrow K^+K^-$ invariant mass spectrum using the kaons identified in the PHENIX detector. The top panel shows the same event (circles) and combinatorial background K^+K^- mass distributions. The bottom panel shows the subtracted mass spectrum fitted with a relativistic Breit-Wigner function convolved with a Gaussian resolution function.

TABLE II. ϕ meson mass centroid and width for the minimum-bias Au+Au collisions at $\sqrt{s_{NN}} = 200$ GeV. The corresponding PDG values are $M_\phi = 1.019456$ GeV/c^2, $\Gamma_\phi = 4.26$ MeV/c^2.

Parameter	Value (MeV/c^2)
Centroid	1.01877 ± 0.00014 (stat) ± 0.00085 (syst)
Width	4.24 ± 0.45 (stat) $\pm \frac{0.55}{0.51}$ (syst)

spectrum (lower panel), containing approximately 5100 ϕ mesons in the fit region, is fitted with a relativistic Breit-Wigner (RBW) mass distribution function [38] convolved with a Gaussian experimental mass resolution function. Using Monte Carlo studies based on the experimentally measured single-kaon momentum resolution, the experimental ϕ mass resolution is calculated to be 1.0 MeV/c^2. This pair mass resolution value is found to be almost constant across the kinematic region of acceptance.

The errors on the data points in Fig. 8 reflect the statistical errors only. The systematic errors associated with the mass centroid and width measurements originate from the magnetic field uncertainties in the kaon momentum determination and the combinatorial background normalization procedure. The minimum-bias line-shape parameters (centroid and width) derived in our analysis are listed in Table II. The fitted minimum-bias ϕ mass centroid and width are consistent at the one standard deviation (1σ) level with the PDG values [55], taking into account both systematic and statistical errors. The centroids and widths from the mass spectra of the three independent subsystem combinations are also found to be consistent with PDG values within errors.

We investigated the centrality dependence of the ϕ meson line shapes. For each centrality bin, we again fitted the ϕ mass spectrum with the RBW function convolved with a Gaussian experimental ϕ mass resolution. The results are presented in Fig. 9. The left panel of the figure shows the centrality dependence of the fitted centroids. The upper and lower 1σ systematic error limits are indicated. The dotted line shows the PDG mass centroid. The solid line indicates the result obtained with a one-parameter constant fit through the measured data points. These results lead to two immediate conclusions. First, to within less than 1 MeV/c^2 there is no observed centrality dependence of the ϕ meson mass centroid, and second, the fitted centroids at all centralities are consistent with the PDG value within the statistical and systematic uncertainties of our measurements.

The ϕ mass widths, as shown in the right panel of the figure, are studied as a function of the centrality. The error bar on each point shows the statistical error; the bands on the points indicate the systematic errors. The dotted line shows the PDG ϕ mass width. The solid line shows the results of the constant-fit assumption to the data points. Again, within the statistical and systematic error limits shown, there is no convincing evidence of a variation of the ϕ width as a function of centrality.

The topic of medium effects on meson masses has been actively investigated in the recent literature [7–10,20,23,56–58]. The predictions are that for both cold and hot nuclear matter there could be a decrease of the ϕ mass value by a few MeV/c^2 or even tens of MeV/c^2. Even more dramatically the width could increase by several multiples above the PDG value of 4.26 MeV/c^2. A sample of such predictions is given in Table III. However, one of the models [20] considers the $\phi \to K^+K^-$ channel largely insensitive to medium effects since the kaons are "unlikely to escape without reacting further, thus destroying any useful information possessed about the ϕ." In this sense the $\phi \to K^+K^-$ is inherently biased in that only ϕ decays that are unaffected by the medium changes, for example those produced peripherally, can be detected.

It is sometimes thought that because the vacuum $c\tau$ of the ϕ is ≈ 45 fm/c there will be only limited sensitivity to medium effects in any case. However, if the resonance width were to actually increase by several times, as indicated in Table III, then the $c\tau$ would then approach or be even substantially less than 10 fm/c, which is a size compatible with the expected collision volume. The dramatic width changes predicted in either cold or hot nuclear matter might be visible, at least in the dilepton channel if not also the K^+K^- channel, as a function of centrality.

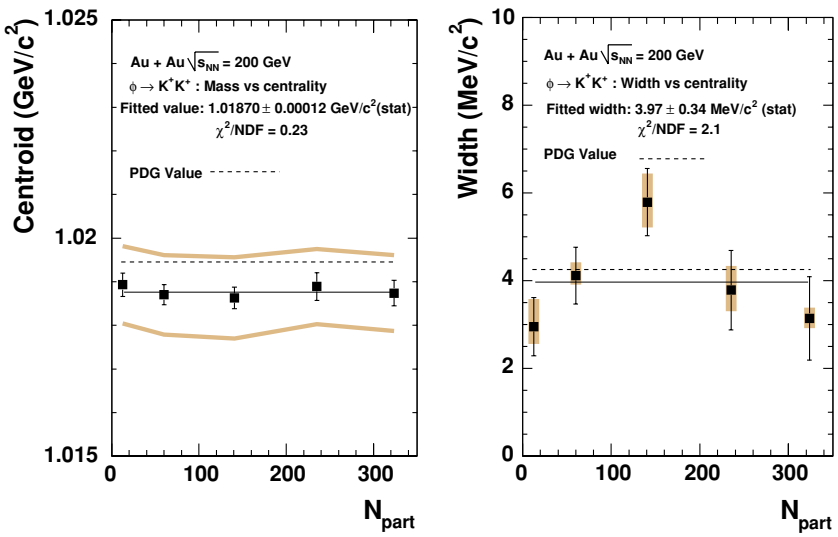

FIG. 9. (Color online) Centrality dependence of the ϕ mass centroid (left panel) and ϕ intrinsic width (right panel), where the $N_{\rm part}$ to Centrality correspondence is given in Table I. For the mass centroid plot, the 1σ systematic error limits on the data points are shown by the two continuous bands. The dotted line shows the PDG centroid value (1.019456 GeV/c^2). The solid line indicates the centroid value obtained from a one-parameter-fit assumption. For the width plot the systematic errors on the RBW widths are indicated as bands on each data point. Similarly, the dotted line shows the PDG width value (4.26 MeV/c^2), and the solid line shows a one-parameter-fit result for the measured data points.

TABLE III. Theoretical predictions for changes in the ϕ resonance.

Authors	Models	Environment	Predictions
Caberara and Vicente Vacas [23]	Chiral SU(3)	Cold hadronic	$M_\phi \rightarrow 1.011$ Gev $\Gamma_\phi \rightarrow 30\,\mathrm{MeV}/c^2$
Pal, Ko, and Lin [13]	AMPT Chiral Lagrangian	Hot hadronic	$M_\phi \rightarrow 0.95\,\mathrm{GeV}/c^2$ at twice normal nuclear density (ρ_0) $\Gamma_\phi \rightarrow 45$ MeV/c^2 at $2\rho_0$ Suppression of $\phi \rightarrow K^+K^-$ relative to $\phi \rightarrow e^+e^-$
Oset and Ramos [21]	Kaon mass renormalization	Cold hadronic	M_ϕ unchanged $\Gamma_\phi \rightarrow 22$ MeV/c^2
Smith and Haglin [20]	One-Boson exchange	Hot hadronic	M_ϕ unchanged $\Gamma_\phi \rightarrow 14$–$24$ MeV/c^2
Blaizot and Mendez Galain [12]	Nambu-Jona-Lasino	Hot hadronic	$M_\phi \rightarrow 2M_K$ at $T \approx T_{\mathrm{critical}}$ Γ_ϕ *reduced* by a factor of 6 $\phi \rightarrow K^+K^-$ disappears
Bi and Rafelski [14]	Bag model Chiral invariance	Hot hadronic	$M_\phi \rightarrow 1.029\,\mathrm{GeV}/c^2$ at $T \approx T_{\mathrm{critical}}$ $\Gamma_\phi \rightarrow 10$ MeV/c^2

The present mass centroid and width data, which are integrated over the available m_T range, rule out any major changes with respect to the PDG values. Specifically, the one-parameter fit result of 3.97 ± 0.34 MeV/c^2 obtained here excludes at the 99% confidence level a width value of 4.75 MeV/c^2 or greater. Possibly at the lowest m_T values, where the ϕ would remain longer in the collision volume, or with the availability of more finely binned centralities, there could be visible evidence of in-medium effects. However, the current data sample is insufficient to explore these possibilities.

It seems clear from the current set of theoretical models that an observed change in the ϕ width would not be itself indicative of a QGP formation. One would first have to constrain the cold nuclear medium effects on the ϕ as could be obtained in d+Au collisions, or by comparing peripheral Au+Au collision data results with central collision data. It is also important to measure the ϕ mass in the dilepton e^+e^- channel. That channel should be more sensitive to the ϕ that are produced deeper or earlier in the collision volume.

B. Spectral-shapes analysis

At low m_T, the spectral shapes carry information about the kinetic freeze–out conditions. Since the centrality dependence reveals the effect of the system size on the fireball evolution it becomes desirable to study the centrality dependence of the spectral shapes. Transverse mass spectra were obtained in three centrality bins corresponding to 0–10%, 10–40%, and 40–92% of the total geometrical cross section. We count the same event K^+K^- pairs within a defined mass window (± 5 MeV/c^2 with respect to the ϕ mass centroid) and estimate the number of combinatorial background pairs within that window. In each centrality bin, the data are divided into different m_T bins. The invariant mass spectrum for the same events and the background distributions are obtained for each of these m_T bins. Finally, the background is subtracted from the same-event invariant mass spectrum within the aforementioned ± 5 MeV/c^2 ϕ mass window to determine the number of reconstructed ϕ mesons within that m_T bin. The reconstruction of the ϕ in the Monte Carlo simulation takes into account the effect of the ϕ mass window size.

The ϕ mesons are reconstructed using kaons identified in the TOF and the PbSc detectors. Three detector combinations (TOF-TOF, TOF-PbSc, and PbSc-PbSc) are used to obtain three independent transverse mass spectra. Figure 10 shows the minimum-bias m_T spectra for these three combinations. The combined result, which is the weighted sum of the three combinations, is also included. For better visibility of the data points, TOF-TOF, TOF-PbSc, and PbSc-PbSc spectra are

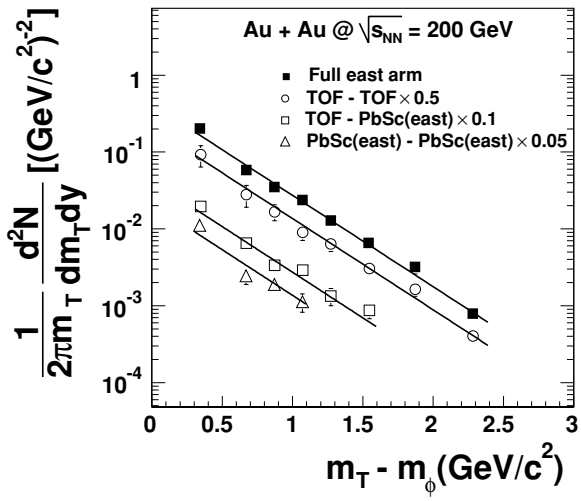

FIG. 10. Minimum-bias m_T spectra of the measured ϕ mesons for three different PHENIX subsystem combinations, with scale factors as indicated. The combined spectrum is fitted with an exponential function in m_T, Eq. (3). The lines drawn through the individual spectra (TOF-TOF, TOF-PbSc, and PbSc-PbSc) represent the same fit parameters as in the minimum-bias case. Statistical error bars are shown.

TABLE IV. Minimum-bias dN/dy and T for different subsystem combinations. The statistical and systematic errors are shown after the first and second $\pm$ signs, respectively.

Subsystem Combination	TOF-TOF	TOF-PbSc	PbSc-PbSc	Full Data Set
dN/dy	$1.16 \pm 0.17 \pm 0.19$	$1.37 \pm 0.15 \pm 0.22$	$1.47 \pm 0.26 \pm 0.27$	$1.34 \pm 0.09 \pm 0.21$
T (MeV)	$380 \pm 18 \pm 22$	$385 \pm 34 \pm 28$	$311 \pm 47 \pm 65$	$366 \pm 11 \pm 18$

scaled by a factor of 0.5, 0.1, and 0.05, respectively. The m_T spectrum obtained from the PHENIX detector is fitted with the exponential function

$$\frac{1}{2\pi m_T}\frac{d^2N}{dm_T dy} = \frac{dN/dy}{2\pi T(T+M_\phi)} e^{-(m_T - M_\phi)/T}, \qquad (3)$$

where dN/dy and the inverse slope T are returned as two fitting parameters. The lines drawn through the TOF-TOF, TOF-PbSc, and PbSc-PbSc spectra represent the same fit but are scaled with the same scaling factors as the data points. Comparison of the individual spectra to the fit obtained from the combined spectrum demonstrates the consistency among the different measurements, which have different systematic uncertainties. The TOF-TOF, TOF-PbSc, and PbSc-PbSc spectra are also independently fitted using Eq. (3). The resulting dN/dy and T are tabulated in Table IV. Both statistical and systematic errors are quoted. The systematic errors on dN/dy originate from the systematic uncertainties associated with extraction of the yields in each m_T bin (see Appendix C) and the uncertainties from the fitting procedure. The latter is sensitive to the extrapolation of the m_T spectra to $m_T = m_\phi$. A detailed account of systematic errors on dN/dy and T in the full dataset from all sources is shown in Appendix C. We also fitted the TOF-TOF and TOF-PbSc data over the smaller m_T range of the PbSc-PbSc data and obtained consistent sets of dN/dy and T values from that check.

Figure 10 and Table IV indicate that the three different analyses with different systematic uncertainties give consistent results. This allowed us to combine the results and make use of the maximum available statistics in each m_T bin. This combined spectrum was used to obtain the physics results discussed in the next sections.

Figure 11 shows m_T spectra of the ϕ mesons in 0–10%, 10–40%, 40–92%, and minimum-bias centrality classes. The data points representing the invariant yield as a function of transverse momentum are given in Appendix B. Each spectrum is fitted with an m_T-exponential function, Eq. (3). The ϕ yield per unit of rapidity (dN/dy) and inverse slope (T) obtained from the fits are shown in Table V and are summarized in Figs. 12 and 13 [59].

C. Yields and ratios

Hadron yields and ratios carry information about the chemical properties of the system. The yields of strange particles have been of particular interest as they help in understanding the strangeness enhancement in heavy-ion collisions and the equilibration of strangeness. It is important to study these phenomena as a function of system size. Centrality-selected data can be particularly useful in this respect. Here we present the yield of the ϕ mesons at midrapidity as a function of centrality and compare this yield to the yields of other hadrons and the results from lower energy heavy-ion collisions. The dN/dy of ϕ (shown in Fig. 12) is found to increase steadily with centrality. In the right panel, the yield is normalized to the number of participant pairs to take into account the size of the system. Within the error bars this normalized rapidity density is approximately independent of centrality with a possible slight increase from peripheral to the midperipheral collisions. The trend is quite different from lower energy results measured at the AGS. In [38], the yield of ϕ was reported to be increasing greater than linearly with the number of participants.

We now consider the ratio of strange to nonstrange particles to understand the extent and mechanism of the strangeness enhancement in heavy-ion collisions. The ratios K^+/π^+ and K^-/π^- are shown in Figs. 14 (a) and (b). Both ratios show an increase of $\approx$60% from peripheral to central collisions. Most of this increase is for $N_{\rm part} < 100$. Only a mild increase or saturation is observed from midcentral to the top centrality bin [50]. Figures 14 (c) and (d) show the centrality dependence of the ϕ/π and ϕ/K ratios. The limited statistics prevent us from extending the ϕ measurements into larger number of centrality bins spanning the more peripheral events. The ϕ/K ratio, in this limited number of centrality bins, is approximately flat as a function of centrality. The possibility of structure in the

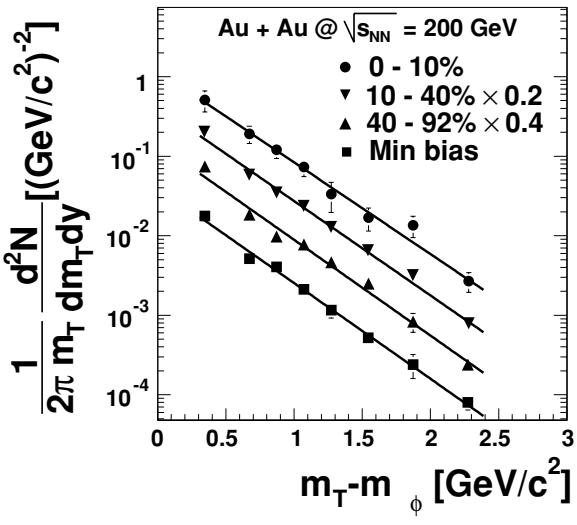

FIG. 11. m_T spectra of ϕ mesons for 0–10%, 10–40%, 40–92%, and minimum-bias (0–92%) centrality classes, with scale factors as indicated. Each spectrum is fitted with an exponential function in m_T, Eq. (3), with the fit parameters listed in Table V. Statistical error bars are shown.

TABLE V. dN/dy and T for different centrality bins.

Centrality (%)	dN/dy	T (MeV)
0–10	3.94 ± 0.60 (stat) ± 0.62 (syst)	376 ± 24 (stat) ± 20 (syst)
10–40	2.22 ± 0.18 (stat) ± 0.35 (syst)	360 ± 13 (stat) ± 23 (syst)
40–92	0.32 ± 0.03 (stat) ± 0.05 (syst)	359 ± 15 (stat) ± 16 (syst)
Minimum Bias	1.34 ± 0.09 (stat) ± 0.21 (syst)	366 ± 11 (stat) ± 18 (syst)

ϕ/π ratio is difficult to infer from our data within the error bars. One might expect to see some centrality dependence in the ϕ/π ratio because there is obviously a centrality dependence to the K/π ratio. However, we do not have enough centrality bins, nor enough signal in each bin, from which to conclusively identify a centrality dependence in ϕ/π. The flat behavior of the ϕ/K ratio indicates that there is no pronounced difference in the production of open (kaon) and hidden (ϕ) strangeness in heavy ion collisions at RHIC energies. Production in the hadronic stage via kaon coalescence $K^+K^- \rightarrow \phi$ seems to be excluded by these data, as it would result in an increase in ϕ/K^- as a function of N_{part}, which is not observed.

The collision energy dependence of the ϕ yield is shown in Fig. 15, where we plot the dN/dy per participant pair as a function of the number of participants for different colliding energies. The figure indicates two aspects of ϕ meson production at various energies. First, as we go from AGS to SPS to RHIC, the ϕ meson yield per participant increases by an order of magnitude overall. Secondly, at the AGS energy, we find a steady increase of ϕ production per participant pair from peripheral to central collisions. It is worth mentioning that the NA50 experiment [25] at CERN SPS reported an increase in fiducial ϕ yield (in the $\mu^+\mu^-$ decay channel) per participant from peripheral to central collisions although the yield per participant showed saturation within the error for the top centrality bins. The yield of ϕ mesons at RHIC, on the contrary, is found to be almost independent of centrality.

To investigate further the mechanism of ϕ enhancement with increase in collision energy, we study the two ratios ϕ/π and ϕ/K^- as a function of collision energy as illustrated in Fig. 16. The ϕ/π ratio is found to increase with the collision energy from AGS to RHIC. The ϕ/K^- ratio, in contrast, remains almost constant within the error bar with increasing collision energy.

D. Hydrodynamical model fits to the spectral-shape data

From the ϕ spectral data shown in the preceding sections, we can conclude that the transverse mass distributions are well described by an exponential distribution and are quite similar for all the centralities. There is little, if any, centrality dependence of the inverse slope parameter in the measured centrality bins, as shown in Fig. 13. The exponential behavior is expected for particle production from a thermal source.

If the system develops collective motion, particles experience a velocity boost resulting in an additional transverse kinetic energy component. This motivates the use of the transverse kinetic energy (i.e., transverse mass minus the particle rest mass) for studying flow effects. Traditionally, the CERN experiments [60,61] have used simple exponential fits to the transverse kinetic energy distributions and often quote just one number, the inverse slope T, to characterize the spectra. These fits are usually done in the range $(m_T - m_0) < 1$ GeV/c^2 to minimize the contribution from hard processes.

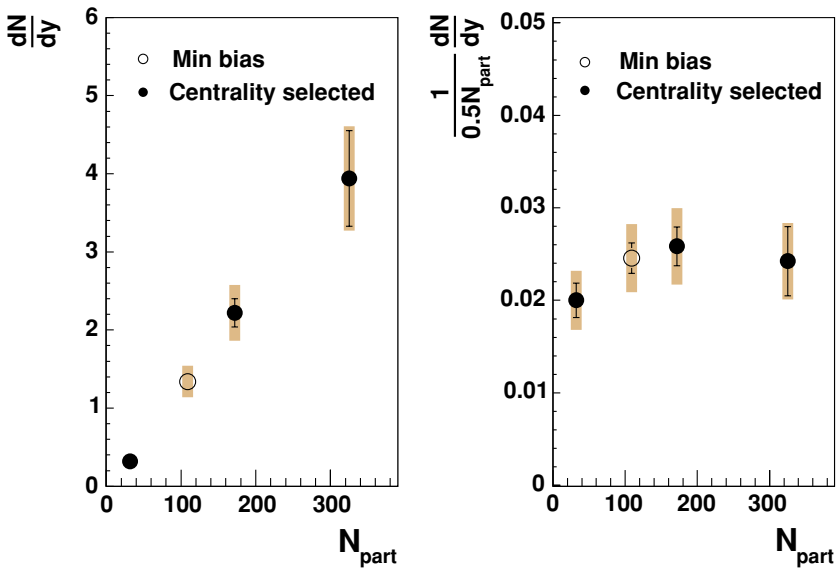

FIG. 12. (Color online) Centrality dependence of ϕ yield at midrapidity. The value of dN/dy increases steadily with the number of participants N_{part} (left) whereas the dN/dy per participant pairs increases slightly from peripheral to midcentral events and saturates after that (right). The error bars indicate the statistical errors. The shaded boxes on each data point are the systematic errors.

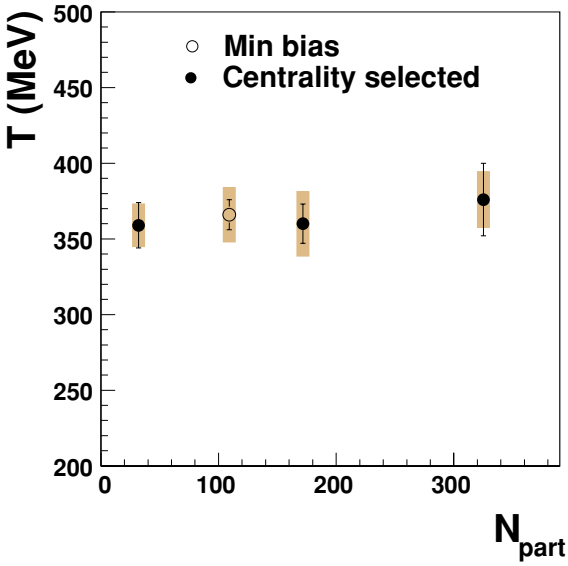

FIG. 13. (Color online) Centrality dependence of the inverse slope T.

The results of such fits, obtained from previously published PHENIX $\pi^{\pm}$, $K^{\pm}$, p, and $\overline{p}$ data [50] are shown in Fig. 17. The slope parameters show a clear mass dependence, as expected from radial flow. The mass dependence increases from peripheral to central collisions, indicating stronger collectivity in the more central events. The ϕ meson has mass similar to that of the proton. Hence we expect that if the ϕ participates in the collective flow then its inverse slope will be affected by this motion. For protons, the slope parameter changes significantly from peripheral to central collisions. As just noted, the ϕ inverse slopes show no such centrality dependence. An important difference between the results obtained for p, $\overline{p}$, and ϕ is that those for the proton and antiproton have been fitted within a limited low-m_T range [$(m_T - m_0) < 1$ GeV/c^2] as motivated by the previous discussion. In the case of the ϕ the full measured range has been used for the fit because of the limited data at low m_T. As shown in Fig. 11, the three data points below 1 GeV/c^2 are consistent with the fit over the entire m_T range.

The detailed study of the higher statistics (anti)proton spectra [50] indicated that (anti)proton spectra cannot be described by a single exponential in $m_T - m_0$, if the full measured range is considered. Although easy to visualize, the one-parameter inverse-slope analysis proves to be too simplistic as a way to infer the kinetic properties of the system. In particular, the degree to which the ϕ mesons participate in the collective expansion will be shown (see Fig. 22) to be obscured in this simple approach.

A more sophisticated approach to this problem is to compare the particle spectra to a functional form that describes a boosted thermal source, based on relativistic hydrodynamics [62]. This is a two-parameter model, termed the "blast-wave" model, in which the surface radial flow velocity (β_T) and the freeze-out temperature ($T_{\rm fo}$) are extracted from the invariant

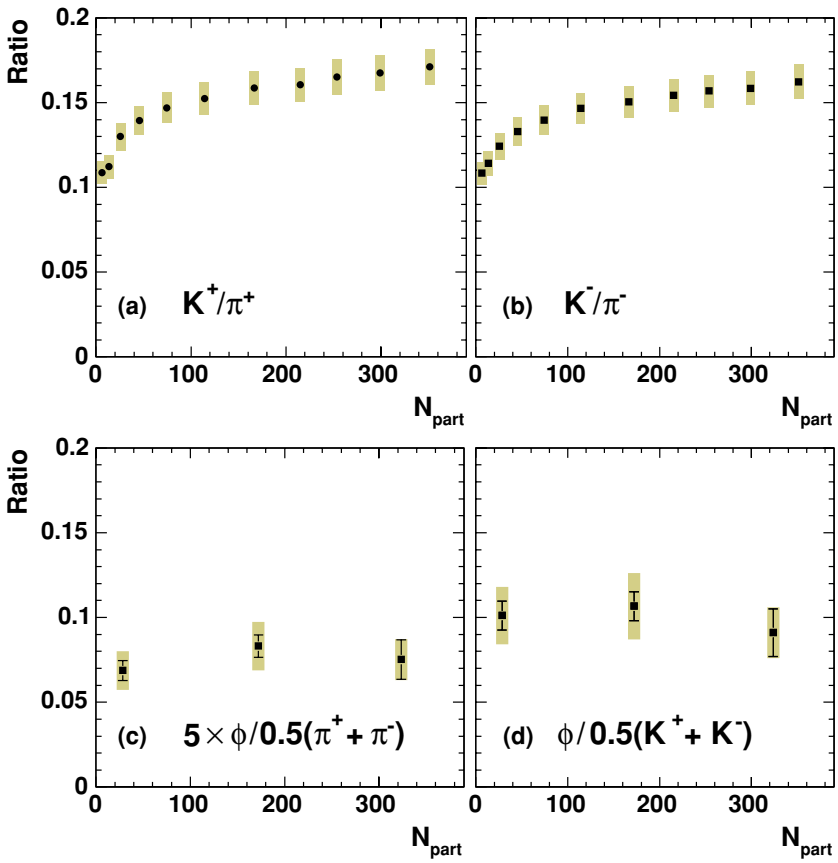

FIG. 14. (Color online) Centrality dependence of particle ratios for (a) K^+/π^+, (b) K^-/π^-, (c) $\phi/[0.5(\pi^+ + \pi^-)]$ (scaled by a factor of 5), and (d) $\phi/[0.5(K^+ + K^-)]$ in Au+Au collisions at $\sqrt{s_{NN}} = 200$ GeV. The data points have been placed in the center of each centrality bin. An increase in ϕ production, similar to kaons, would shift the lowest bin slightly to the right by about 20% to an $N_{\rm part}$ of about 40, in (c).

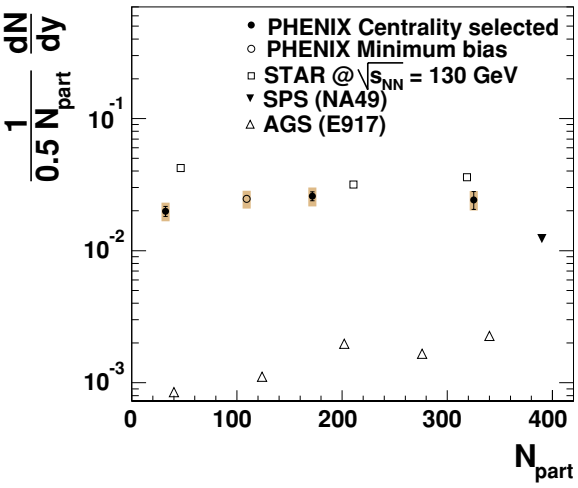

FIG. 15. (Color online) Centrality dependence of ϕ yields at different collision energies. STAR data are from [43], NA49 data are from [39], and E917 are from [38].

cross-section data according to the equation

$$\frac{dN}{m_T\, dm_T} \propto \int_0^R f(r)\, r\, dr m_T I_0\left(\frac{p_T \sinh\rho}{T_{\rm fo}}\right) K_1\left(\frac{m_T \cosh\rho}{T_{\rm fo}}\right), \tag{4}$$

where I_0 and K_1 represent modified Bessel functions with ρ being the transverse boost, which depends on the radial position according to

$$\rho = \tanh^{-1}(\beta_T) r/R. \tag{5}$$

Here the parameter R is the maximum radius of the expanding source at freeze-out. The function $f(r)$ represents the density, which is taken to be uniform in this calculation. A detailed comparison between our implementation of the blast-wave model and the results of full hydrodynamics calculations has been reported previously in [63] and the results were found to be consistent.

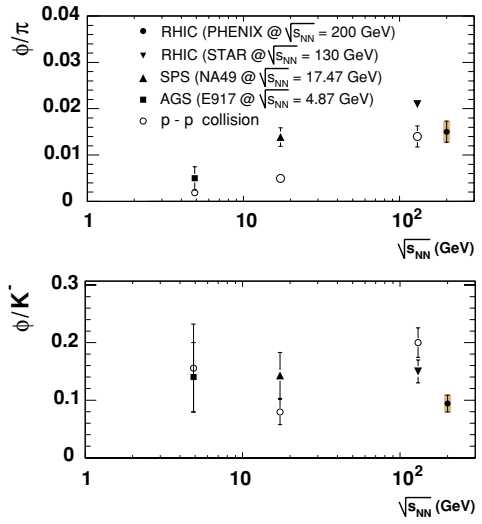

FIG. 16. (Color online) ϕ/π (top) and ϕ/K^- (bottom) ratios as a function of collision energy. The data symbols have the same meanings in both the top and the bottom parts of the figure.

To study the parameter correlations, we make a grid of ($T_{\rm fo}$, β_T) pairs and then for each pair we perform a chi-squared minimization for each particle type. We use a linear velocity profile and constant particle density distribution. The first fit attempt is performed simultaneously for the six particle species $\pi^{\pm}$, $K^{\pm}$, p, and $\overline{p}$ in the range $(m_T - m_0) < 1.0$ GeV/c^2.

The experimental data for p and $\overline{p}$ have been corrected for Λ and $\overline{\Lambda}$ decays. However, the invariant yields of $\pi^{\pm}$ and $K^{\pm}$ include feed-down from the decay of resonances and weak decays. To take this into account we add the decay of mesonic (ρ, η, ω, K^*, . . .) and baryonic (Δ, Λ, Σ, . . .) resonances as follows:

(1) Generate resonances with the transverse momentum distribution determined by each combination of $T_{\rm fo}$ and β_T.
(2) Simulate the decays using a Monte Carlo approach and obtain $\pi^{\pm}$ and $K^{\pm}$ distributions.
(3) Merge all particles, where the particle abundance is calculated with chemical parameters [64]$T_{\rm ch} = 177$ MeV, $\mu_B = 29$ MeV.

The two-parameter $T_{\rm fo}$ versus β_T fit results obtained in this analysis for the most central bin are shown in Fig. 18. Shown in the lower panel of the figure are the χ^2 contour levels obtained from fitting each particle spectrum separately. We observe that the parameters $T_{\rm fo}$ and β_T are anticorrelated; the different particles have different preferred parameter space and different sensitivity to the parameters. For example, the contours for the heavier particles are more sensitive to the flow velocity than to the kinetic freeze-out temperature. The minimum valleys in the contours for the six particle species do overlap at a single common point at the 2σ level. To find the values of the parameters at this overlap point, a simultaneous fit for the six single-particle spectra ($\pi^{\pm}$, $K^{\pm}$, p, and $\overline{p}$) was done; the result converges to a best fit value of $T_{\rm fo} = 108.9^{+2.6}_{-2.4}$ MeV and $\beta_T = 0.771^{+0.003}_{-0.004}$. Using these parameters, we obtain the transverse momentum shapes shown in Fig. 19, where we also include the prediction for the ϕ spectrum shape, which was not part of the original fit. The shape of the ϕ spectrum is reproduced well.

For the two other centrality bins in this study, 10–40% and 40–92%, we show the best-fit hydrodynamical results in Figs. 20 and 21, respectively. Again we see that the ϕ transverse momentum shapes are reproduced by the same flow parameters that fit the identified hadron data at the same centrality bins.

For a second hydrodynamical fit attempt, we include the ϕ transverse momentum 0–10% centrality data along with the previously identified hadron data as part of the χ^2 minimization search. The flow parameters derived with the ϕ data included are numerically consistent with the flow parameters derived previously without the ϕ data being included.

The two-dimensional grid-search best-fit values for the blast-wave parametrization as a function of centrality are tabulated in Table VI. The radial average expansion velocity $\langle\beta_T\rangle$ is also given in this table. For the range of centralities studied here, the expansion velocity parameter is seen to decrease moderately for more peripheral collisions whereas

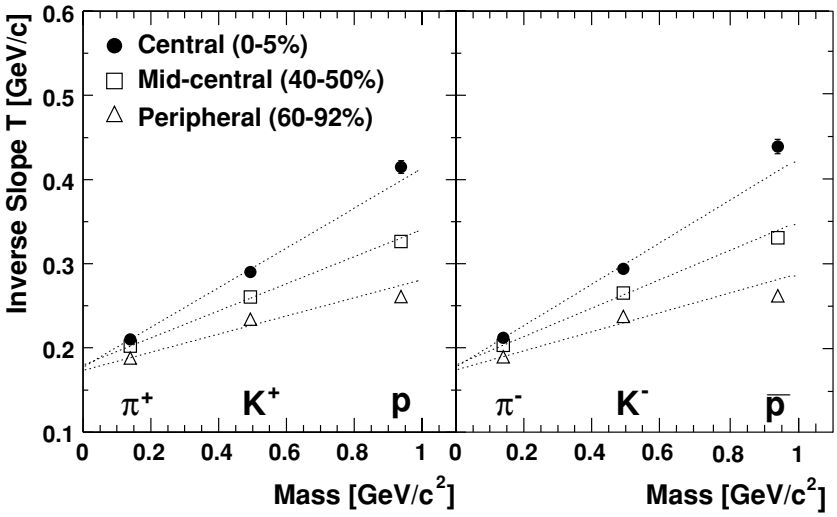

FIG. 17. Mass and centrality dependence of inverse slope parameters T in m_T spectra for positive (left) and negative (right) particles in Au+Au collisions at $\sqrt{s_{NN}} = 200$ GeV. The fit ranges are 0.2–1.0 GeV/c^2 for pions and 0.1–1.0 GeV/c^2 for kaons, protons, and antiprotons in $m_T - m_0$. Figure taken from Ref. [50].

the kinetic freeze-out temperature increases more significantly, by approximately 40%. If one takes these parameters literally, then the more peripheral collisions are subject to decreased radial flow while correspondingly the particles are decoupling kinetically from each other at temperatures closer to the chemical freeze-out temperature. This is a physically reasonable scenario given fewer participants in the initial expansion phase.

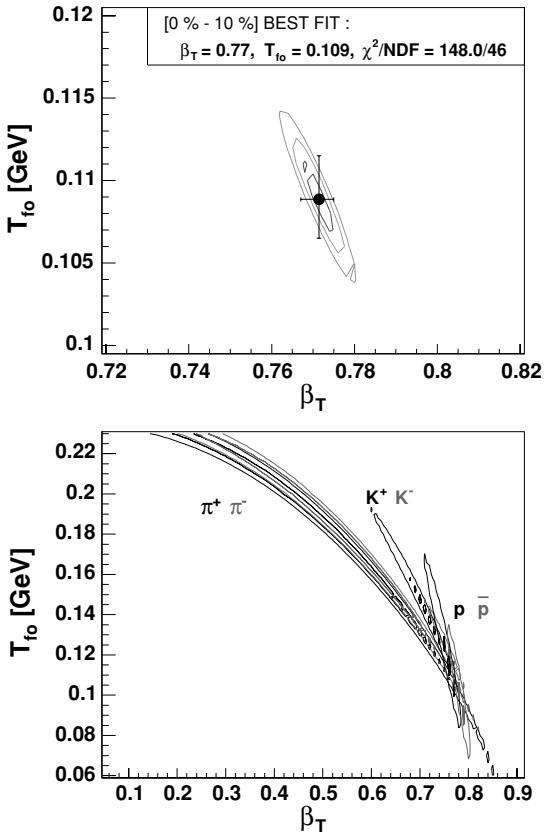

FIG. 18. (Color online) Contour plots for the hydrodynamical fit to the 200-GeV single-particle transverse momentum spectra for the $\pi^{\pm}$, $K^{\pm}$, p, and $\overline{p}$ in the 0–10% centrality bin. The contour lines are in 1σ steps. The upper plot is from a simultaneous fit with the best value shown as the dot. The lower plot is from independent fits for the six-particle spectra.

It should be pointed out that our present ϕ transverse momentum range does not extend below 0.8 GeV/c. The spectral shapes at low m_T, especially for the heavier particles, are mostly sensitive to the expansion velocity. In the range of our ϕ measurement, it is more appropriate to consider the asymptotic behavior of the spectral shapes, which for $m_T \gg m_0$ is given by [62]

$$T_{\text{eff}} = T_{\text{fo}}\sqrt{(1+\beta_T)/(1-\beta_T)}, \tag{6}$$

where T_{eff} is the slope parameter obtained using an m_T exponential fit, as in Eq. (3). It is interesting to note that the measured asymptotic slopes do not seem to depend on centrality, although both T_{fo} and β_T show a clear centrality dependence. This either is due to a cancellation effect in Eq. (6), since the parameters are anticorrelated, or indicates that the hydrodynamics description is no longer valid at these large transverse momenta. We conclude that although the ϕ data themselves cannot constrain the kinematic freeze-out conditions, they are consistent with the hydrodynamical results obtained from the simultaneous fit to the $\pi^{\pm}$, $K^{\pm}$, p, and $\overline{p}$ spectra.

TABLE VI. Blast-wave-model parameters [62] as a function of centrality from fitting $\pi^{\pm}$, $K^{\pm}$, p, and $\overline{p}$ spectra. The fit parameters quoted here are the results from fitting the six identified hadrons spectra simultaneously, without including the ϕ.

Centrality (%)	T_{fo} [MeV]	β_T	$\langle\beta_T\rangle$	χ^2/NDF
0–10	$108.9^{+2.6}_{-2.4}$	$0.771^{+0.003}_{-0.004}$	$0.572^{+0.003}_{-0.003}$	148.0/46
10–40	$119.0^{+1.5}_{-1.5}$	$0.748^{+0.003}_{-0.003}$	$0.550^{+0.002}_{-0.002}$	212.1/46
40–92	150^{+2}_{-2}	$0.630^{+0.005}_{-0.005}$	$0.447^{+0.004}_{-0.004}$	150.9/46

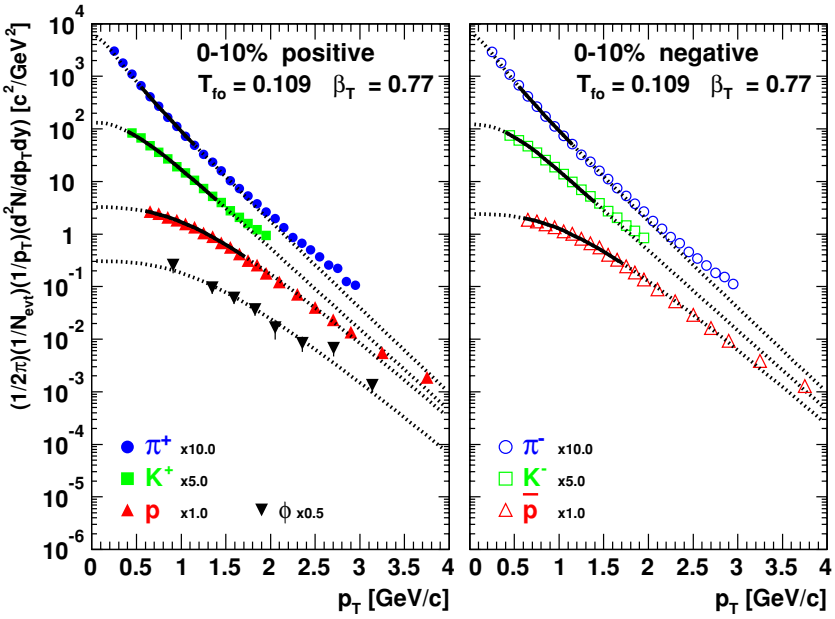

FIG. 19. (Color online) Transverse momentum data and best-fit hydrodynamical results for the 0–10% centrality bin for the 200-GeV $\pi^{\pm}$, $K^{\pm}$, p, and $\overline{p}$, along with the prediction for the ϕ transverse momentum spectrum. The transverse momentum ranges for the fit are indicated by the solid lines; the dashed lines indicate the extrapolated predictions for each particle species.

E. Nuclear modification factor R_{CP} for ϕ mesons

One of the most important result demonstrated so far in the study of relativistic heavy ions at RHIC is the observed suppression of high-p_T pions in central collisions as compared to either pp collisions or peripheral Au+Au collisions [65]. A second, quite surprising observation is the unusually large (anti)proton-to-pion ratio at high p_T. In particular, PHENIX has observed [30] that in central Au+Au collisions the p/π and $\overline{p}/\pi$ ratios are enhanced by a factor of 3 at intermediate p_T ($1.5 < p_T < 4.5$ GeV/c) as compared to the ratios in pp collisions and the ratios obtained in quark and gluon jets measured in e^+e^- collisions [66]. It was also observed that proton and antiproton production scales with $N_{\rm coll}$ in this p_T region, in sharp contrast to the strong suppression of pion production [30]. In pp collisions high-p_T particles are the result of the fragmentation of partons. Because of the power-law nature of the hard-scattering spectrum, most of the particles at high p_T are expected to be leading hadrons. The fragmentation functions, at least in vacuum, are expected to be universal and independent of the colliding system under consideration. However, at intermediate p_T (1.5–4.5 GeV/c) the PHENIX results from central Au+Au collisions are inconsistent with the known fragmentation functions.

There are several conjectures that may explain the unexpected PHENIX result:

(1) hydrodynamic flow generated from the hadronic stage [67],

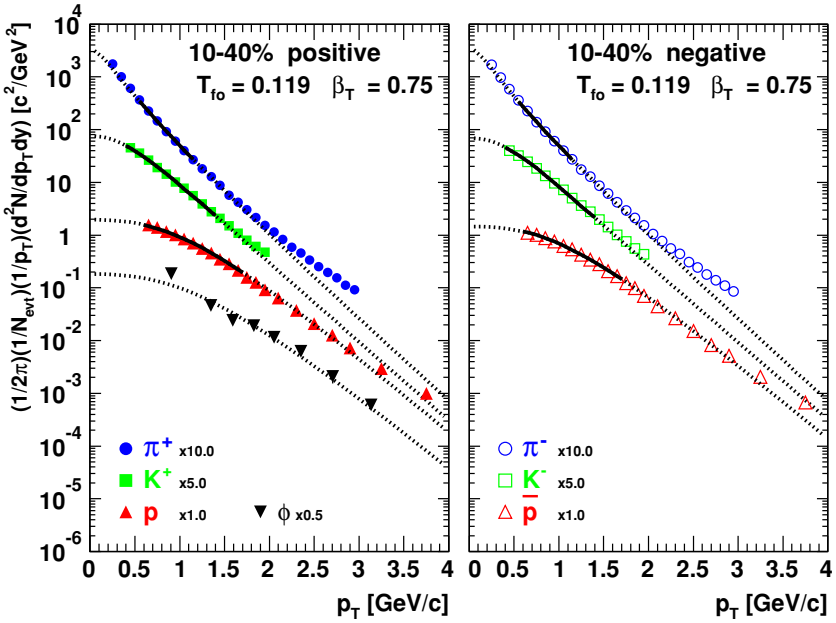

FIG. 20. (Color online) Transverse momentum data and best-fit hydrodynamical results for the 10–40% centrality bin for the 200-GeV $\pi^{\pm}$, $K^{\pm}$, and p, $\overline{p}$, along with the prediction for the ϕ transverse momentum spectrum.

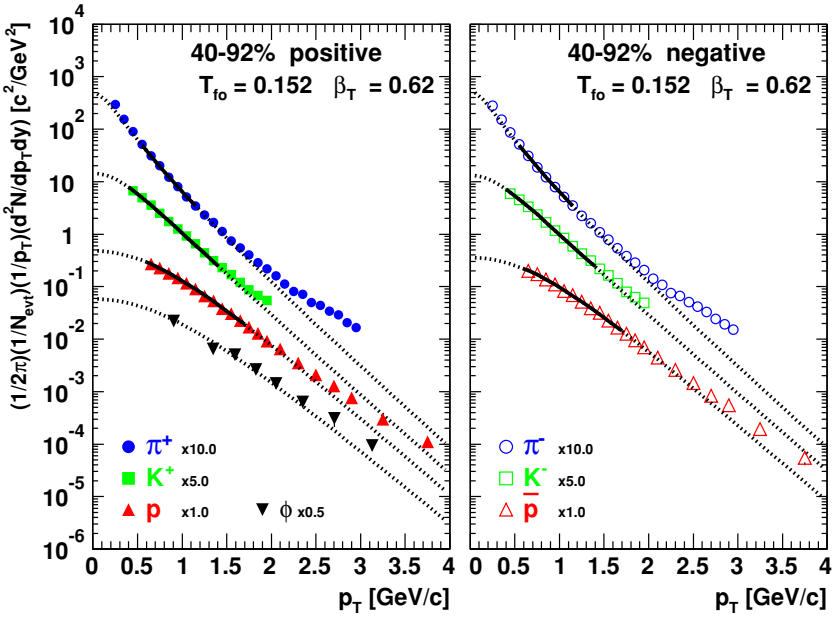

FIG. 21. (Color online) Transverse momentum data and best-fit hydrodynamical results for the 40–92% centrality bin for the 200-GeV $\pi^{\pm}$, $K^{\pm}$, and p, $\overline{p}$, along with the prediction for the ϕ transverse momentum spectrum.

(2) hydrodynamic flow generated at a partonic stage together with particle production from the recombination [32–34],
(3) baryon junctions as a mechanism for an usually large buildup of baryons and antibaryons at midrapidity [68], or
(4) in-medium modified fragmentation functions [69].

The first three possibilities invoke soft processes to populate a region of p_T that is dominated by hard scattering in pp collisions. The soft production at intermediate p_T is enhanced for protons and antiprotons, whereas pions remain dominated by hard scattering. In conjecture 4, the production for both pions and p, $\overline{p}$ is by hard scattering, but the fragmentation functions are modified in the medium, thus resulting in enhanced p/π and $\overline{p}/\pi$ ratios.

The second of these conjectures is particularly important since this hypothesis presupposes a partonic state with collective behavior. A critical factor that may differentiate among these scenarios is whether the large abundance of protons is due to its mass or to the number of constituent quarks [32–35]. Hydrodynamic flow generated at the hadronic stage imparts a single velocity to the moving matter; hence similar mass particles should exhibit the same momentum increase from this effect. In contrast, hypotheses 2 and 3 depend on whether the particles are baryons or mesons.

The ϕ meson which has a mass similar to that of a proton yet, like the pion, has two constituent quarks, should distinguish between conjecture 1 and 2 or 3. We examine the scaling properties of the intermediate-p_T yields of the ϕ and compare those to the yields of $(p + \overline{p})/2$. Figure 22 shows the transverse momentum spectra measured in three different centralities, each scaled down by the number of binary nucleon-nucleon collisions. The (anti)proton spectra show two pronounced features. Below $p_T < 1.5$ GeV/c, the spectral shapes are strongly influenced by the radial flow and thus the more central data have a harder slope. Above $p_T = 1.5$ GeV/c, the effect of radial flow is negligible. The spectra converge to the same line. Moreover, they scale with $N_{\rm coll}$ for all centrality classes, as expected for hardscattering unaffected by the nuclear medium. The ϕ spectra have a quite different behavior. There is no visible curvature at lower p_T. This could be because the ϕ spectra have only two (rather wide) bins below $p_T = 1.5$ GeV/c—the region where the curvature in the proton spectra is most pronounced. A curved functional form can be fit to the spectra with acceptable χ^2, as already discussed in Sec. IV D. At higher p_T the ϕ spectra run parallel to the (anti)proton spectra, but they do not obey $N_{\rm coll}$ scaling. To examine this feature on a linear scale, we plot the ratio between the central and peripheral data, that is, the ratio $R_{\rm CP}$

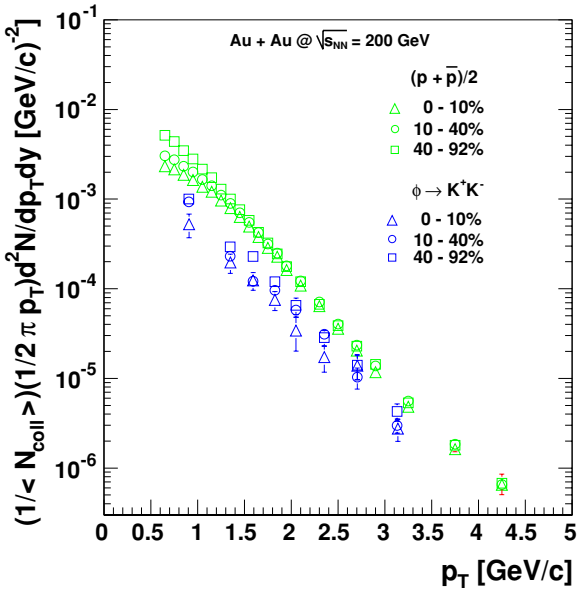

FIG. 22. (Color online) p_T spectra of protons and ϕ mesons at different centralities scaled down by their respective number of $N_{\rm coll}$.

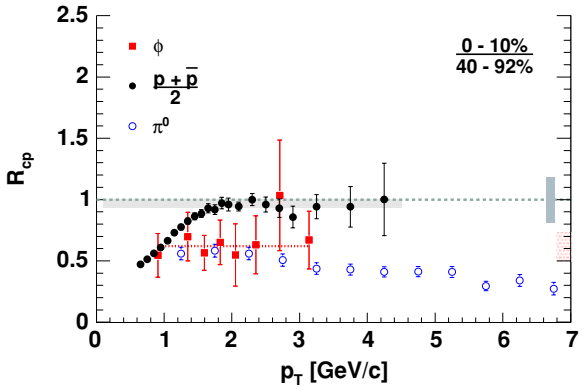

FIG. 23. (Color online) $N_{\rm coll}$ scaled central to peripheral ratio $R_{\rm CP}$ for $(p+\overline{p})/2$, π^0, and ϕ. The proton and pion results are published [30]. The vertical dotted bar on the right represents the error on $N_{\rm coll}^{0-10\%}/N_{\rm coll}^{40-92\%}$. The shaded solid bar around $R_{\rm CP}=1$ represents 12% systematic error, which can move the proton and/or ϕ points with respect to one another. The dotted horizontal line at $R_{\rm CP}=0.62$ is a straight-line fit to the ϕ data.

(Fig. 23). The systematic error arising from the determination of $N_{\rm coll}$ is about 19%. It is common for all three particle species shown in the figure, because the nuclear modification factors were obtained from the same centrality classes. The dotted horizontal line at $R_{\rm CP}=0.62$ is a straight-line fit to the ϕ data. To facilitate the comparison between the proton results and the ϕ including systematic errors, the $N_{\rm coll}$ error is plotted in two places: with a solid bar around $R_{\rm CP}=1$ and with a dotted bar around $R_{\rm CP}=0.62$. Since these errors are correlated, if the curves in the figure were to change owing to a change in the value of $N_{\rm coll}$, they will move together up or down within the extent of the error bars shown. We would like to emphasize the *comparison* between the $R_{\rm CP}$ values for the protons and the ϕ. In this comparison, the systematic errors in determining $N_{\rm coll}$ cancel. The important systematic errors to consider are those that can move the ϕ points with respect to the proton points. When determining a ratio of spectra measured at different centralities, most systematic errors cancel. After removing the $N_{\rm coll}$ error, the sources of error that remain for the ϕ come from the multiplicity-dependent corrections and the effect of the mass window as described previously. For the protons and pions [29,30], the error that remains that is independent of the error determined for the ϕ comes from the multiplicity-dependent corrections. The relative error between the ϕ and the proton measurements is evaluated at 7% and is represented by the extended solid bar just below $R_{\rm CP}=1$. Clearly, the ϕ's behavior is more like that of the pions and not like that of the protons. Thus we conclude that the ϕ meson exhibits a suppression effect at intermediate p_T similar to that of the pions. Although we cannot conclude whether ϕ production at this intermediate p_T is dominated by soft or hard processes, this observation provides support for models that depend on the number of constituent quarks in the particle as opposed to models that depend on just the mass of the particle to explain the anomalous proton yields. Other RHIC data on this subject are reviewed in Ref. [70].

V. CONCLUSIONS

A systematic measurement has been made of ϕ production at midrapidity in Au+Au collisions with $\sqrt{s_{NN}}=200$ GeV at RHIC. The general features of the data include the yield, which rises from 0.318 ± 0.028 (stat) $\pm$ 0.051 (syst) in peripheral collisions to 3.94 ± 0.60 (stat) $\pm$ 0.62 (syst) in central collisions. There is seen to be little centrality dependence to the inverse slope, which is about 360 MeV. The centroid mass and resonance width are extracted with high enough precision to rule out any large (MeV/c^2 scale) deviations from the accepted PDG values. At p_T below 1.5 GeV/c, a blast-wave analysis of the most central pion, kaon, and proton spectra with a freeze-out temperature $T_{\rm fo}$ of 109 MeV and a transverse velocity β_T of 0.77 describes the most central ϕ data as well. A similar conclusion, with monotonically changing results for $T_{\rm fo}$ and β_T, holds for the less central events. At higher transverse momenta, all particles lie above the blast-wave fits, which suggests that the dominant particle production mechanism is no longer soft physics but is giving way to the expected jet fragmentation. A study of the ratio $R_{\rm CP}$ of the ϕ provides a critical new piece of information in understanding the anomalous proton-to-pion ratio seen in central heavy ion collisions at RHIC, since the ϕ is a meson with a mass similar to that of a proton. The $R_{\rm CP}$ value for the ϕ above a transverse momentum of 1.5 GeV/c is about 0.6, similar to that of the pions but inconsistent with the proton value of 1. This indicates that the ϕ meson is being suppressed in this p_T range for the more central collisions. The lower p_T blast-wave fits imply hydrodynamic behavior at the hadronic stage, whereas the inconsistency with simple hydrodynamics at higher p_T is something one would expect in the jet fragmentation region. This transition is an important factor to consider as one begins to understand the mechanism of particle production in central collisions at RHIC.

ACKNOWLEDGMENTS

We thank the staff of the Collider-Accelerator and Physics Departments at Brookhaven National Laboratory and the staff of the other PHENIX participating institutions for their vital contributions. We acknowledge support from the Department of Energy, Office of Science, Nuclear Physics Division, the National Science Foundation, Abilene Christian University Research Council, Research Foundation of SUNY, and the Dean of the College of Arts and Sciences at Vanderbilt University (U.S.A); Ministry of Education, Culture, Sports, Science, and Technology and the Japan Society for the Promotion of Science (Japan); Conselho Nacional de Desenvolvimento Científico e Tecnológico and Fundação de Amparo à Pesquisa do Estado de São Paulo (Brazil); Natural Science Foundation of China (People's Republic of China); Centre National de la Recherche Scientifique, Commissariat à l'Énergie Atomique, Institut National de Physique Nucléaire et de Physique des Particules, and Institut National de Physique Nucléaire et de Physique des Particules (France); Bundesministerium für Bildung und Forschung, Deutscher Akademischer Austausch Dienst, and Alexander von Humboldt Stiftung (Germany); Hungarian

National Science Fund, OTKA (Hungary); Department of Atomic Energy and Department of Science and Technology (India); Israel Science Foundation (Israel); Korea Research Foundation and Center for High Energy Physics (Korea); Russian Ministry of Industry, Science and Tekhnologies, Russian Academy of Science, and Russian Ministry of Atomic Energy (Russia); VR and the Wallenberg Foundation (Sweden); the U.S. Civilian Research and Development Foundation for the Independent States of the Former Soviet Union; the US-Hungarian NSF-OTKA-MTA; the US-Israel Binational Science Foundation, and the 5th European Union TMR Marie-Curie Programme.

APPENDIX A: COMBINATORIAL BACKGROUND

Assume there are N tracks per event of which n are positive and $N-n$ are negative, the probability of the partition being $P(n)$ such that $\sum_{n=0}^{N} P(n) = 1$.

All the following expressions refer to the average number of pairs per event

1. General relation between the number of like and unlike pairs

The total number of pairs is

$$N_{\text{pairs}} = \frac{N(N-1)}{2}. \tag{A1}$$

The number of $+-$ pairs is

$$n_{+-} = \sum_{n=0}^{N} n(N-n)P(n) = N\langle n\rangle - \langle n^2\rangle. \tag{A2}$$

The number of $++$ pairs is

$$n_{++} = \sum_{n=0}^{N} \frac{n(n-1)}{2} P(n) = \frac{\langle n^2\rangle - \langle n\rangle}{2}. \tag{A3}$$

The number of $--$ pairs is

$$n_{--} = \sum_{n=0}^{N} \frac{(N-n)(N-n-1)}{2} P(n) \tag{A4}$$

$$= \frac{N(N-1)}{2} - \left(N - \frac{1}{2}\right)\langle n\rangle + \langle n^2\rangle. \tag{A5}$$

We therefore get

$$n_{++} + n_{--} = \frac{N(N-1)}{2} - (N\langle n\rangle - \langle n^2\rangle). \tag{A6}$$

The last expression is trivial: The number of like-sign pairs is equal to the total number pairs minus the number of unlike-sign pairs.

The ratio R of unlike to like pairs is therefore

$$R = \frac{n_{+-}}{n_{++} + n_{--}} = \frac{N\langle n\rangle - \langle n^2\rangle}{N(N-1)/2 - (N\langle n\rangle - \langle n^2\rangle)}. \tag{A7}$$

This is a general result, free of any assumption, and should always be fulfilled, in pure combinatorial background as well as in a mixture of signal plus combinatorial background.

2. Combinatorial background

Consider a pure combinatorial background sample. By its essence there are *no correlations* between tracks in such a sample; that is, within an event the probability p to have a positive (or a negative) track is constant and independent of the number of tracks. Therefore the probability $P(n)$ of having n positive tracks out of the total of N tracks is given by a binomial distribution

$$P(n) = \frac{N!}{n!(N-n)!} p^n (1-p)^{N-n}, \tag{A8}$$

$$\langle n\rangle = pN, \tag{A9}$$

$$\langle n^2\rangle = \sigma^2 + \langle n\rangle^2 = Np(1-p) + p^2N^2. \tag{A10}$$

Replacing these values in expression (6) gives

$$R = \frac{(p-p^2)}{(1/2 - p + p^2)}. \tag{A11}$$

If there is charge symmetry (i.e., $p = 0.5$) one gets $R = 1$ and consequently the combinatorial background is given by

$$n_{+-}^{\text{CB}} = n_{++} + n_{--}. \tag{A12}$$

This is an exact relation. It holds with quite good accuracy even if there is some charge asymmetry. For example, for an asymmetry of 10% (i.e., $p = 0.525$), $R = 0.995$.

3. The formula $N_{+-}^{\text{CB}} = 2\sqrt{N_{++}N_{--}}$

The combinatorial background is rigorously given by this formula provided that the number N of tracks per event has a Poisson distribution:

$$\mathcal{P}(N) = \frac{\langle N\rangle^N e^{-N}}{N!}. \tag{A13}$$

Again we assume that the N tracks are divided into n positive and $N-n$ negative tracks, the partition is given by the binomial distribution (A7), and all expressions to follow refer to average number of pairs per event.

The number of $++$ pairs is

$$N_{++} = \sum_{N=2}^{\infty} \mathcal{P}(N) \sum_{n=0}^{N} P(n) \frac{n(n-1)}{2}. \tag{A14}$$

Using relations (A7) and (A11) and some algebra leads to

$$N_{++} = \tfrac{1}{2} p^2 \langle N\rangle^2. \tag{A15}$$

Similarly, the number of $--$ pairs is given by

$$N_{--} = \sum_{N=2}^{\infty} \mathcal{P}(N) \sum_{n=0}^{N} P(n) \frac{(N-n)(N-n-1)}{2} \tag{A16}$$

$$= \frac{1}{2}(1-p)^2 \langle N\rangle^2. \tag{A17}$$

TABLE VII. m_T spectra of ϕ mesons in different centrality bins. The systematic errors on invariant yields are from combinatorial background normalization, ϕ counting mass window, acceptance correction efficiencies from Monte Carlo and occupancy-dependent corrections.

Centrality (%)	m_T (GeV/c^2)	m_T Bin Size (GeV/c^2)	$\frac{1}{2\pi m_T}\frac{d^2N}{dm_T dy}$ [(GeV^2/c^4)$^{-2}$]	Stat. Error [(GeV^2/c^4)$^{-2}$]	Syst. Error [(GeV^2/c^4)$^{-2}$]
0–10	1.365	0.4	0.51114	0.15120	0.0778747
	1.691	0.2	0.19114	0.04656	0.029121
	1.891	0.2	0.12065	0.02702	0.018382
	2.091	0.2	0.07313	0.01758	0.011142
	2.291	0.2	0.03335	0.01372	0.005081
	2.565	0.4	0.01683	0.00541	0.002564
	2.891	0.2	0.01353	0.00406	0.002061
	3.300	1.0	0.00268	0.00074	0.000408
10–40	1.364	0.4	0.37232	0.04145	0.05667
	1.691	0.2	0.09224	0.01255	0.01404
	1.891	0.2	0.04872	0.00719	0.00742
	2.091	0.2	0.03867	0.00483	0.00589
	2.291	0.2	0.02320	0.00389	0.00353
	2.564	0.4	0.01246	0.00160	0.00189
	2.891	0.2	0.00415	0.00110	0.00063
	3.294	1.0	0.00120	0.00021	0.00018
40–92	1.364	0.4	0.04432	0.00622	0.00645
	1.691	0.2	0.01295	0.00185	0.00189
	1.891	0.2	0.01009	0.00110	0.00147
	2.091	0.2	0.00531	0.00074	0.00077
	2.291	0.2	0.00287	0.00060	0.00042
	2.563	0.4	0.00126	0.00024	0.00018
	2.891	0.2	0.00062	0.00019	0.00009
	3.293	1.0	0.00019	0.00004	0.00003

The number of combinatorial background $+-$ pairs is

$$N_{+-}^{\mathrm{CB}} = \sum_{N=2}^{\infty} \mathcal{P}(N) \sum_{n=0}^{N} P(n) n(N-n) \quad \text{(A18)}$$

$$= p(1-p)\langle N^2 \rangle. \quad \text{(A19)}$$

Inspecting (A15), (A16), and (A17) shows that

$$N_{+-}^{\mathrm{CB}} = 2\sqrt{N_{++}N_{--}}. \quad \text{(A20)}$$

APPENDIX B: DATA TABLES OF CENTRALITY-SELECTED ϕ SPECTRA

The invariant yields, $(\frac{1}{2\pi m_T})(\frac{d^2N}{dm_T dy})$, of the ϕ mesons in different centrality bins are shown in Table VII.

APPENDIX C: SYSTEMATIC ERRORS ON dN/dy, T, AND m_T- SPECTRA

The sources of the systematic errors on yield (dN/dy), T, and m_T- spectra measurements come from the following sources:

(a) Systematic error on the combinatorial background normalization δ_{norm}: This originates from the systematics of the event mixing. Since both same-event and mixed-event like-sign distributions represent pure combinatorials, we estimated unlike-sign combinatorial background by normalizing the mixed-event unlike-sign distributions to $2\sqrt{N_{++}^{\text{Same event}} N_{--}^{\text{Same event}}}$ and $2\sqrt{N_{++}^{\text{Mixed event}} N_{--}^{\text{Mixed event}}}$, and the difference in the extracted ϕ signal from the real data between these two normalizations are attributed to the systematic uncertainty.

TABLE VIII. Systematic error in dN/dy.

Centrality (%)	δ_{norm} (%)	δ_{mass} (%)	δ_{extrap} (%)	δ_{MC} (%)	δ_{occu} (%)	$\delta_{\mathrm{sys}}^{\mathrm{tot}}$ (%)
Minimum Bias	0.7	2.6	4.0	12.4	7.8	15
0–10	0.8	4.2	5.2	12.4	10	17
10–40	1.1	2.3	5.9	12.4	8.5	16
40–92	0.7	3.1	6.0	12.4	7	16

TABLE IX. Systematic error in T.

Centrality (%)	δ_{mass} (%)	δ_{fit} (%)	$\delta_{\mathrm{sys}}^{\mathrm{tot}}$ (%)
Minimum Bias	0.6	4.9	5
0–10	1.1	5.2	5
10–40	1.1	6.2	6
40–92	1.1	4.2	4

We use the same normalization factor for all m_T bins. So, these systematics are applicable to the measured dN/dy only and the absolute normalization of the m_T spectra, but they do not affect their shape and the inverse slope, T.

(b) Systematics of the ϕ mass window, δ_{mass}: We count the number of reconstructed ϕ mesons by integrating the ϕ meson invariant mass spectra within a ± 5 MeV mass window with respect to the measured centroids in both data and Monte Carlo. The systematic associated with this mass window is estimated by measuring the extent of the changes in dN/dy and T after constructing ϕ meson m_T spectra within five different mass windows (± 3, ± 5, ± 8, ± 10, and ± 15 MeV) with respect to the measured ϕ centroids.

(c) Uncertainties in extrapolation of ϕ meson m_T spectra to $m_T = m_\phi$, δ_{extrap}: This is studied by

(i) fitting the m_T distributions with two different fitting functions (exponential and Boltzmann functions) and

(ii) fitting the transverse mass spectra within different m_T ranges. These are applied to both dN/dy and T.

(d) Acceptance correction systematics, δ_{MC}: The systematics associated with acceptance correction factors derived from Monte Carlo analysis are investigated by considering two sources:

(i) tuning of detector alignments in Monte Carlo with reference to the real data ($\sim 3\%$) and

(ii) systematics in the fiducial geometries in data and Monte Carlo ($\sim 12\%$).

The systematic error from this source is independent of the momenta of reconstructed ϕ mesons. So, this is attributed to dN/dy and the absolute normalization of the m_T spectra.

(e) Systematic error in the occupancy-dependent efficiency corrections, δ_{occu}: The systematic error associated with this efficiency is estimated by calculating the occupancy-dependent correction with different track confirmation criteria and is independent of the pair momenta. This systematic effect was shown to be momentum independent and hence affects these normalization of spectra and dN/dy, but not the extracted slope parameters.

These systematic errors are quoted in Tables VIII and IX for dN/dy and T, respectively.

[1] E. Laermann and O. Philipsen, Ann. Rev. Nucl. Part. Sci. **53**, 163 (2003).
[2] J. D. Bjorken, Phys. Rev. D **27**, 140 (1983).
[3] K. Adcox *et al.* (PHENIX Collaboration), Phys. Rev. Lett. **87**, 052301 (2001).
[4] J. Rafelski and B. Müller, Phys. Rev. Lett. **48**, 1066 (1982).
[5] A. Shor, Phys. Rev. Lett. **54**, 1122 (1985).
[6] P. Koch, B. Müller, and J. Rafelski, Phys. Rep. **142**, 167 (1986).
[7] C. P. Singh, Phys. Rev. Lett. **56**, 1750 (1986).
[8] C. P. Singh, Phys. Lett. **B188**, 369 (1987).
[9] C. P. Singh, Phys. Rep. **236**, 147 (1993).
[10] C. P. Singh, *et al.*, Phys. Lett. **B393**, 188 (1997).
[11] S. A. Bass *et al.*, Nucl. Phys. **A661**, 205 (1999).
[12] J.-P. Blaizot and R. Mendez Galain, Phys. Lett. **B271**, 32 (1991).
[13] S. Pal, C. M. Ko, and Z. Lin, Nucl. Phys. **A707**, 525 (2002).
[14] P. Bi and J. Rafelski, Phys. Lett. **B262**, 485 (1991).
[15] M. Asakawa and C. M. Ko, Nucl. Phys. **A572**, 732 (1994).
[16] C. Song, Phys. Lett. **B388**, 141 (1996).
[17] M. Asakawa and C. M. Ko, Phys. Lett. **B322**, 33 (1994).
[18] C. M. Ko and D. Seibert, Phys. Rev. C **49**, 2198 (1994).
[19] K. Haglin, Nucl. Phys. **A584**, 719 (1995).
[20] W. Smith and K. L. Haglin, Phys. Rev. C **57**, 1449 (1998).
[21] E. Oset and A. Ramos, Nucl. Phys. **A679**, 616 (2001).
[22] S. Okubo, Phys. Lett. **B5**, 165 (1963).
[23] D. Cabrera and M. J. Vicente Vacas, Phys. Rev. C **67**, 045203 (2003).
[24] S. Eidelman *et al.*, Phys. Lett. **B592**, 11 (2004).
[25] B. Alessandro *et al.*, Phys. Lett. **B555**, 147 (2003).
[26] V. Friese *et al.*, Nucl. Phys. **A698**, 487 (2002).
[27] K. Adcox *et al.* (PHENIX Collaboration), Phys. Rev. Lett. **88**, 022301 (2002).
[28] K. Adcox *et al.* (PHENIX Collaboration), Phys. Lett. **B561**, 82 (2003).
[29] S. S. Adler *et al.* (PHENIX Collaboration), Phys. Rev. Lett. **91**, 072303 (2003).
[30] S. S. Adler *et al.* (PHENIX Collaboration), Phys. Rev. Lett. **91**, 172301 (2003).
[31] K. Adcox *et al.* (PHENIX Collaboration), Phys. Rev. Lett. **88**, 242301 (2002).
[32] R. J. Fries, B. Müller, C. Nonaka, and S. A. Bass, Phys. Rev. C **68**, 044902 (2003); Phys. Rev. Lett. **90**, 202303 (2003).
[33] R. C. Hwa and C. B. Yang, Phys. Rev. C **70**, 024905 (2004).
[34] V. Greco, C. M. Ko, and P. Lévai, Phys. Rev. C **68**, 034904 (2003).
[35] V. Greco, C. M. Ko, and P. Lévai, Phys. Rev. Lett. **90**, 202302 (2003).
[36] Y. Akiba *et al.*, Phys. Rev. Lett. **76**, 2021 (1996).
[37] H. Fesefeldt *et al.*, Nucl. Phys. **B147**, 317 (1979); D. Drijard *et al.*, Z. Phys. C. **9**, 293 (1981), and references therein.
[38] B. B. Back *et al.* (E917 Collaboration), Phys. Rev. C **69**, 054901 (2004).
[39] S. V. Afanasiev *et al.* (NA49 Collaboration), Phys. Lett. **B491**, 59 (2000).
[40] M. C. Abreu *et al.* (NA38 Collaboration), Phys. Lett. **B368**, 239 (1996).
[41] M. C. Abreu *et al.* (NA50 Collaboration), Phys. Lett. **B555**, 147 (2003); **B561**, 294(E) (2003).
[42] D. Rohrich *et al.*, J. Phys. G **27**, 355 (2001).
[43] C. Adler *et al.* (STAR Collaboration), Phys. Rev. C **65**, 041901(R) (2002).
[44] K. Adcox *et al.* (PHENIX Collaboration), Nucl. Instrum. Methods A **499**, 469 (2003).
[45] M. Aizawa *et al.* (PHENIX Collaboration), Nucl. Instrum. Methods A **499**, 508 (2003).
[46] L. Aphecetche *et al.* (PHENIX Collaboration), Nucl. Instrum. Methods A **499**, 521 (2003).

[47] M. Allen *et al.* (PHENIX Collaboration), Nucl. Instrum. Methods A **499**, 549 (2003).
[48] C. Adler, A. Denisov, E. Garcia, M. Murray, H. Stroebele, and S. White, Nucl. Instrum. Methods A **470**, 488 (2001).
[49] K. Adcox *et al.* (PHENIX Collaboration), Nucl. Instrum. Methods A **499**, 489 (2003).
[50] S. S. Adler *et al.* (PHENIX Collaboration), Phys. Rev. C **69**, 034909 (2004).
[51] J. T. Mitchell *et al.*, Nucl. Instrum. Methods A **482**, 491 (2002).
[52] The mass squared for each track is defined as $M^2 = p^2(t^2c^2/L^2 - 1)$, where p is the momentum, t is the time of flight, c is the speed of light, and L is the length of the path traversed by the track from vertex to the detector.
[53] L. Aphecetche *et al.*, Nucl. Instrum. Methods A **499**, 521 (2003).
[54] GEANT 3.21, CERN program library.
[55] The PDG value for the ϕ mass centroid is $1019.456 \pm 0.020\,\mathrm{MeV}/c^2$, and for the ϕ width the value is $4.26 \pm 0.05\,\mathrm{MeV}/c^2$ [24].
[56] F. Klingl, T. Waas, and W. Weise, Phys. Lett. **B431**, 254 (1998).
[57] R. Rapp and J. Wambach, Adv. Nucl. Phys. **25**, 1 (2000), edited by A. Perlmutter, J. W. Negele, and E. W. Vogt (Kluwer Academic Publishers).
[58] L. Alvarez-Ruso and V. Koch, Phys. Rev. C **65**, 054901 (2002).
[59] The STAR experiment at RHIC has recently reported its analysis of the $\phi \to K^+K^-$ data for Au+Au at $\sqrt{s_{NN}} = 200$ GeV [71]. The analyses for PHENIX and STAR have one common centrality bin, 0–10%, for which the extracted dN/dy are not in agreement. The STAR value is $6.65 \pm 0.35\,(\mathrm{stat}) \pm 0.73\,(\mathrm{sys})$, compared with the PHENIX value $3.94 \pm 0.60\,(\mathrm{stat}) \pm 0.62\,(\mathrm{sys})$. The discrepancy persists even if one eliminates the four lowest m_T data points from the STAR data set to fit over the same m_T range for both the STAR and the PHENIX data. There is not a discrepancy between the quoted inverse slope parameters.
[60] I. G. Bearden *et al.* (NA44 Collaboration), Phys. Rev. Lett. **78**, 2080 (1997); H. Boggild *et al.*, Phys. Rev. C **59**, 328 (1999); I. G. Bearden *et al.*, Phys. Lett. **B388**, 431 (1996); I. G. Bearden *et al.*, Phys. Rev. C. **57**, 837 (1998).
[61] E. Andersen *et al.* (WA97 Collaboration), J. Phys. G **25**, 171 (1999).
[62] E. Schnedermann, J. Sollfrank, and U. Heinz, Phys. Rev. C **48**, 2462 (1993).
[63] K. Adcox *et al.* (PHENIX Collaboration), Phys. Rev. C **69**, 024904 (2004).
[64] P. Braun-Munzinger, D. Magestro, K. Redlich, and J. Stachel, Phys. Lett. **B518**, 41 (2001).
[65] S. Adler *et al.* (PHENIX Collaboration), Phys. Rev. C **69**, 034910 (2004).
[66] P. Abreu *et al.* (DELPHI Collaboration), Eur. Phys. J. C **17**, 207 (2000).
[67] T. Hirano and Y. Nara, Nucl. Phys. **A743**, 305 (2004); T. Hirano and K. Tsuda, Phys. Rev. C **66**, 054905 (2002); D. Teaney, J. Lauret, and E. V. Shuryak, Phys. Rev. Lett. **86**, 4783 (2001); P. Kolb *et al.*, Nucl. Phys. **A696**, 197 (2001); P. Huovinen *et al.*, Phys. Lett. **B503**, 58 (2001).
[68] G. C. Rossi and G. Veneziano, Nucl. Phys. **B123**, 507 (1977); D. Kharzeev, Phys. Lett. **B378**, 238 (1996); S. E. Vance, M. Gyulassy, and X.-N. Wang, *ibid.* **B443**, 45 (1998); I. Vitev and M. Gyulassy, Phys. Rev. C **65**, 041902(R) (2002).
[69] X-.N. Wang, Nucl. Phys. **A702**, 238 (2002).
[70] J. Velkovska, J. Phys. G **30**, S835 (2004).
[71] J. Adams *et al.* (STAR Collaboration), Phys. Lett. **B612**, 181 (2005).